
SYMPLECTIC NEURAL FLOWS FOR MODELING AND DISCOVERY

Priscilla Canizares*, Davide Murari*, Carola-Bibiane Schönlieb*, Ferdia Sherry*, Zakhar Shumaylov*

*Department of Applied Mathematics and Theoretical Physics, University of Cambridge
{pc464, dm2011, cbs31, fs436, zs334}@cam.ac.uk

ABSTRACT

Hamilton’s equations are fundamental for modeling complex physical systems, where preserving key properties such as energy and momentum is crucial for reliable long-term simulations. Geometric integrators are widely used for this purpose, but neural network-based methods that incorporate these principles remain underexplored. This work introduces `SympFlow`, a time-dependent symplectic neural network designed using parameterized Hamiltonian flow maps. This design allows for backward error analysis and ensures the preservation of the symplectic structure. `SympFlow` allows for two key applications: (i) providing a time-continuous symplectic approximation of the exact flow of a Hamiltonian system—purely based on the differential equations it satisfies, and (ii) approximating the flow map of an unknown Hamiltonian system relying on trajectory data. We demonstrate the effectiveness of `SympFlow` on diverse problems, including chaotic and dissipative systems, showing improved energy conservation compared to general-purpose numerical methods and accurate approximations from sparse irregular data.

Keywords Deep learning · Physics-informed · Dynamical systems · Hamiltonian systems · Symplectic maps · Symplectic integrators · Neural Flows

1 Introduction

Recent advances have demonstrated the ability of machine learning models to predict dynamics from time series data [47, 25], solve differential equations in an unsupervised manner [36, 46], learn Hamiltonian or Lagrangian structures from data [26, 19, 16, 33], and symbolically discover underlying differential equations [5, 15, 17]. While promising, the applicability of these methods is often hindered by challenges related to trainability [35], scalability [27], and the specific complexities of the systems under consideration [42].

A key challenge in numerically solving differential equations is preserving critical physical quantities of interest, such as energy or momentum. Numerically reproducing a solution’s qualitative behavior is often essential for obtaining reliable long-term predictions. General-purpose numerical solvers frequently fail in doing so.

To address this problem, there is a thorough study of geometric integrators [28], specifically designed to preserve first integrals of motion or other properties of the underlying system. Similar geometric extensions for neural network-based integrators remain underdeveloped. This, coupled with the inherent errors in learned models, leads to error propagation that becomes increasingly severe over time. As a result, effectively training such models becomes a significant challenge [30, 35], hindering the feasibility of long-term simulations [58, 41, 43].

This work introduces `SympFlow`, a neural flow constrained to be symplectic by construction. The symplectic constraint enables it to provide accurate and reliable long-term solutions for Hamiltonian systems. `SympFlow` is a universal approximator in the space of Hamiltonian flows (Theorem 1) and its architecture permits the extraction of the exact “shadow” Hamiltonian corresponding to the neural flow (Equation (6)). This facilitates backward analysis through Hamiltonian matching and allows for error-free switching between the Hamiltonian and flow representations. This flexibility makes our approach adaptable to diverse tasks, including unsupervised learning scenarios where the objective is to solve a given Hamiltonian differential equation, and supervised settings where the network learns to evolve a system solely based on observed trajectories. In essence, `SympFlow` acts as both: (i) a Hamiltonian neural network [26] capable of error-free evolution, and (ii) a neural flow [4] from which the underlying Hamiltonian can be extracted. We demonstrate the efficacy of `SympFlow` across a range of supervised and unsupervised tasks, including those involving noise and dissipation.

1.1 Outline of the paper

This paper is structured as follows: Section 1.2 provides an overview of related work. Section 2 introduces SympFlow¹, detailing its architecture, discussing the various training approaches and in Section 3 we prove various theoretical properties related to SympFlow. Finally, Section 4 presents the numerous experimental results demonstrating its effectiveness and usefulness for long-term stable integration, both in the *supervised* and *unsupervised* settings. We conclude with Section 5 summarizing our findings and expanding on future research directions.

1.2 Related Work

Deep Learning Integrators The deep learning revolution has profoundly impacted scientific computing, particularly in simulating physical systems governed by differential equations.

Physics-Informed Neural Networks (PINNs) [36, 46, 57] have emerged as a prominent approach, integrating domain knowledge, physical laws, and constraints directly into the learning process. PINNs have been demonstrated effective in solving forward and inverse problems for partial differential equations (PDEs) [46, 52, 64, 34, 49] and regularizing learning [60].

Among the efforts in using PINNs to solve differential equations, we mention in particular the works [29, 40], where the authors focus on applying these techniques to Hamiltonian systems. Both of these papers focus on solving a single initial value problem, i.e., they fix an initial condition, and do not constrain their neural networks to reproduce the expected qualitative behavior of the Hamiltonian flow, such as being symplectic.

The surge in interest in PINNs stems from the limitations of traditional numerical solvers, which often struggle with computationally demanding scenarios, such as high-dimensional problems, non-linear and non-smooth PDEs requiring expensive fine grid discretization, and the need for repeated simulations across varying domain geometries, parameters, and different initial and boundary conditions [31].

Incorporating physical constraints, such as energy conservation, within PINNs has led to the development of structured neural networks [8, 22, 32, 10], for example enforcing point symmetry equivariance into the network architectures [2, 37, 48]. It is crucial to note that while PINNs leverage physical constraints for regularization, they do not typically enforce these constraints explicitly within their architecture. This contrasts with our work, which does not follow a PINN-based strategy but focuses on constructing *neural networks that intrinsically preserve the symplectic structure of the phase space*.

Symplecticity in Neural Networks In recent years, there has been a surge of research dedicated to integrating symplectic structures into neural networks modeling Hamiltonian systems. These efforts can be broadly classified into two categories: *fixed-step* and *variable-step* methods, with significant variations in how the symplectic structure is used.

Fixed-step methods explicitly construct a symplectic mapping between consecutive time steps. Examples include SympNet [32], and HénonNet [6], which can interface with separable and non-separable Hamiltonian systems. Despite the symplectic constraint, these networks are universal approximators within the space of symplectic maps [32, 53] and lead to controlled prediction errors [11].

Variable-step methods predominantly utilize a Hamiltonian Neural Network (HNN) [26] or Neural ODE [13] framework. HNNs directly learn the Hamiltonian function, ensuring the recovery of conservative dynamics. Conversely, Neural ODEs recover continuous dynamics by integrating neural network-based differential equations. Both approaches often rely on general-purpose numerical methods, which can disrupt the symplectic structure and the conservative nature of the system.

To address this, several works embed symplectic integrators within the network architecture. Notable examples include SRNN [14], TaylorNet [54], SSINN [20], and NSSNN [59]. SymODEN [63] further extends this framework by incorporating an external control term into the Hamiltonian dynamics. These methods aim to predict continuous system trajectories while preserving the symplectic structure of the phase space.

However, in the broader literature, recent research in neural flows [4] has demonstrated significant improvements in long-time integration compared to Neural ODE counterparts, without the use of numerical solvers. This motivates our extension of fixed-step methods, particularly SympNets [32], to the flow framework. By directly learning the Hamiltonian flow-map and being able to associate it with an exact analytical Hamiltonian function, the analysis is considerably simplified, circumventing the need for intricate procedures, for example, through discrete gradients [39].

¹Code will be made public upon acceptance.

In a similar fashion to `SympFlow`, also the `TSympOCNet` network architecture in [61] is a time-dependent symplectic neural network. Both these two architecture take inspiration from `SympNets`, and introduce a time-dependency modifying its architecture. Our work departs from [61] in how the time-dependency is introduced and also in the focus of the research. While our work aims to theoretically analyse the properties of the proposed model, and experimentally evaluate its effectiveness compared to unconstrained networks, the focus of [61] is on developing a model to be used in the context of path planning problems.

While this review is not exhaustive, it is worth noting the existence of alternative approaches such as learning modified generating functions as symplectic map representations [12], or directly addressing constrained Hamiltonian systems [21, 9].

Non-conservative systems Real-world dynamical systems often exhibit energy dissipation due to irreversible processes such as heat transfer, friction, and radiation. Accurately capturing such dynamics necessitates incorporating these effects into the equations of motion.

While neural networks have shown promise in modeling conservative Hamiltonian systems, extending these approaches to non-conservative dynamics presents significant challenges. Existing efforts primarily focus on augmenting the Hamiltonian framework. Within the context of HNNs and NODEs, one approach involves the separate parameterization of the Hamiltonian and the dissipative term [50]. Another more prevalent approach leverages the framework of port-Hamiltonian dynamics. For instance, [18] extends Hamiltonian Neural Networks (HNNs) to port-Hamiltonian systems, while [62] adapts `SymODEN` to this framework.

However, to the best of our knowledge, no prior work addresses non-conservative dynamics within the context of symplectic flows.

This work adopts a distinct and simpler strategy based on the formulation proposed by [23, 24]. This formulation recasts non-conservative dynamics within a classical Hamiltonian framework by doubling the phase-space variables and computing the evolution equations in the corresponding doubled space. The counterparts of the phase-space variables follow a time-reversed trajectory, thus keeping the total energy of the augmented system constant. The final form of the solution is obtained by projecting back onto the original system, that is, taking the physical limit, recovering the original non-conservative dynamics (see Appendix A for a description of the procedure). This method allows for a unified treatment of conservative and non-conservative systems, enabling direct application of existing neural network architectures and techniques developed for Hamiltonian systems, without explicit modeling of dissipative forces. We have adapted this technique to recast non-conservative dynamics in a symplectic form and seamlessly model dissipation within `SympFlow`.

1.3 Main contributions

The main contributions can be summarized as follows:

- We introduce a novel time-dependent symplectic neural flow, `SympFlow`, designed using parameterized Hamiltonian flow maps. This network can be used both for approximating the flow of a Hamiltonian system, given the governing equations, and learning the underlying Hamiltonian directly from observed trajectory data.
- Theoretically, we show that `SympFlow` is a universal approximator in the space of Hamiltonian flows in Theorem 1. Furthermore, the ability to extract the underlying Hamiltonian from a trained `SympFlow` enables a-posteriori backward analysis of the approximated system in Theorem 2.
- Practically, we demonstrate that `SympFlow` can effectively model and learn both conservative and non-conservative dynamics, preserving the symplectic structure even in the presence of dissipation. This is demonstrated for three systems: a Simple Harmonic Oscillator (Section 4.1), Henon-Heiles (Section 4.3) and Damped Harmonic Oscillator (Section 4.2).
- Numerical examples highlight that `SympFlow` exhibits improved long-term energy behavior compared to unstructured neural networks and is more data efficient in supervised learning tasks.

2 Methodology

In this work we focus on canonical Hamiltonian systems, that is systems of ordinary differential equations (ODEs) of the form:

$$\frac{dx}{dt} = \mathbf{J}\nabla H(x), \quad \text{with} \quad \mathbf{J} = \begin{pmatrix} 0 & \mathbf{I}_d \\ -\mathbf{I}_d & 0 \end{pmatrix}, \quad (1)$$

for a state variable $x \in \mathbb{R}^{2d}$ and a twice-continuously differentiable *Hamiltonian* function $H : \mathbb{R}^{2d} \rightarrow \mathbb{R}$. In Equation (1), the matrices $\mathbf{I}_d, 0 \in \mathbb{R}^{d \times d}$ are the identity and zero matrices respectively. The phase space variable is typically partitioned into a position $q \in \mathbb{R}^d$ and momentum $p \in \mathbb{R}^d$, $x = (q, p)$. Under standard, non-restrictive, assumptions on H , the corresponding initial value problem has a unique solution for any initial condition and initial time [1], which can be used to define the corresponding time- t *flow map* $\phi_{H,t} : \mathbb{R}^{2d} \rightarrow \mathbb{R}^{2d}$:

$$\frac{d}{dt}\phi_{H,t}(x_0) = \mathbf{J}\nabla H(\phi_{H,t}(x_0)) \quad \text{and} \quad \phi_{H,0}(x_0) = x_0. \quad (2)$$

Time-independent Hamiltonian systems as in Equation (2) conserve the Hamiltonian energy function, i.e., $H(\phi_{H,t}(x_0)) = H(x_0)$ for every $t \geq 0$.

The exact flow map in Equation (2) is generally not accessible, and we have to approximate it. For Hamiltonian systems, the time- t flow is *symplectic* since the Jacobian matrix $D\phi_{H,t}(x)$ satisfies the identity $[D\phi_{H,t}(x)]^\top \mathbf{J} [D\phi_{H,t}(x)] = \mathbf{J}$. Consequently, the flow $\phi_{H,t}$ preserves the canonical phase space volume [28]. It is thus desirable that, when approximating $\phi_{H,t}$, such qualitative properties are reproduced by the approximate map.

2.1 The SympFlow architecture

SympFlow generalizes the gradient modules of SympNets [32] to accommodate time dependence. Each of its layers is the exact time- t flow of a suitable time-dependent Hamiltonian system. This design ensures the approximated Hamiltonian flow retains the essential symplectic structure across layers. More specifically, SympFlow is defined by composing exact flow maps of time-dependent Hamiltonians, each of which depends either on position or momentum, but not both. Hence, given an arbitrary continuously differentiable function $V_q : \mathbb{R} \times \mathbb{R}^d \rightarrow \mathbb{R}$, we can consider the flow map (starting from time 0):

$$\phi_{q,t}(q, p) = \left(p - (\nabla_q V_q(t, q) - \nabla_q V_q(0, q)), \right), \quad (3)$$

which corresponds to the Hamiltonian $H_{q,t}(q, p) = \dot{V}_q(t, q)$, where \dot{V}_q stands for $\partial_t V_q$ and the subscript q indicates that the Hamiltonian depends on position, but not momentum. Similarly, for a continuously differentiable function $V_p : \mathbb{R} \times \mathbb{R}^d \rightarrow \mathbb{R}$, we can consider the flow map (starting from time 0):

$$\phi_{p,t}(q, p) = \left(q + \frac{(\nabla_p V_p(t, p) - \nabla_p V_p(0, p))}{p}, \right), \quad (4)$$

which corresponds to the Hamiltonian $H_{p,t}(q, p) = \dot{V}_p(t, p)$. As above, the subscript p indicates that the Hamiltonian depends on momentum but not position.

Although the Hamiltonians above take a very particular form, they naturally arise when applying splitting integration methods to separable Hamiltonians. This work capitalizes on these methods, which have previously been used to good effect in designing neural networks with desirable structural properties [10]. This connection with separable Hamiltonian systems only provides an intuitive way to interpret the network layers. However, there is no inherent limitation in applying SympFlow to non-separable systems; see Theorem 1. By parameterizing V_q and V_p as multi-layer perceptrons (MLPs) and composing such steps, we obtain a time-dependent symplectic map, the parameters of which can be optimized to perform different tasks such as fitting data and, more generally, minimizing an objective function. A SympFlow $\bar{\psi} : \mathbb{R} \times \mathbb{R}^{2d} \rightarrow \mathbb{R}^{2d}$ with $L \in \mathbb{N}$ layers is a map of the form:

$$\bar{\psi}(t, \cdot) = \phi_{p,t}^L \circ \phi_{q,t}^L \circ \dots \circ \phi_{p,t}^1 \circ \phi_{q,t}^1. \quad (5)$$

We represent one layer of the architecture in Figure 1. We remark that since SympFlow is obtained by composing *exact* flow maps, it satisfies $\bar{\psi}(0, x) = x$ for every point $x \in \mathbb{R}^{2d}$.

In Equation (5), $\phi_{q,t}^i$ denotes the map in Equation (3) where V_q is replaced by a V_q^i , and similarly for $\phi_{p,t}^i$. We will interchangeably use the notation $\bar{\psi}(t, x) = \bar{\psi}_t(x)$ to denote the action of a SympFlow.

2.2 The Hamiltonian of the SympFlow

One of the key properties of our architecture is that it is the composition of Hamiltonian flows. This implies that it is also a Hamiltonian flow, as described by the next proposition.

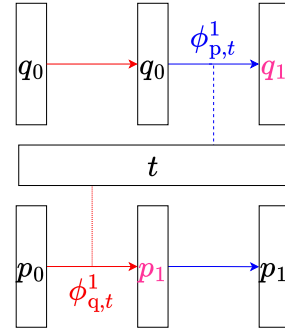


Figure 1: One layer of the SympFlow

Proposition 1 (Proposition 1.4.D [45]). *Let $H^1, H^2 : \mathbb{R} \times \mathbb{R}^{2d} \rightarrow \mathbb{R}$ be continuously differentiable functions, and $\phi_{H^1, t}, \phi_{H^2, t} : \mathbb{R}^{2d} \rightarrow \mathbb{R}^{2d}$ the exact time- t flows (starting from time 0) of the Hamiltonian systems they define. Then, the map $\psi_t = \phi_{H^2, t} \circ \phi_{H^1, t} : \mathbb{R}^{2d} \rightarrow \mathbb{R}^{2d}$ is the exact time- t flow of the Hamiltonian system defined by the Hamiltonian function*

$$H^3(t, x) = H^2(t, x) + H^1\left(t, \phi_{H^2, t}^{-1}(x)\right).$$

Thanks to Proposition 1, we can associate a SympFlow with a time-dependent Hamiltonian function. To assemble such a Hamiltonian function, we can group the pairs of alternated momentum and position flows, finding the Hamiltonian associated with $\phi_{p, t}^i \circ \phi_{q, t}^i$, which is

$$H_t^i(q, p) = \dot{V}_p^i(t, p) + \dot{V}_q^i(t, q - (\nabla_p V_p^i(t, p) - \nabla_p V_p^i(0, p))).$$

The Hamiltonian of the SympFlow in Equation (5) can then be expressed iteratively, aggregating from the last layer to the first as

$$H_t^{L:i}(x) = H_t^{L:(i+1)}(x) + H_t^i\left(\phi_{H_t^{L:(i+1)}, t}^{-1}(x)\right), \quad i = 1, \dots, L-1, \quad (6)$$

where $H_t^{L:L} = H_t^L$, and

$$\phi_{H_t^{L:i}, t}^{-1} = \left(\phi_{H_t^{L:(i+1)}, t} \circ \phi_{H_t^i, t}\right)^{-1} = \phi_{H_t^i, t}^{-1} \circ \phi_{H_t^{L:(i+1)}, t}^{-1}.$$

To lighten the notation, we introduce the operator \mathcal{H} sending a SympFlow $\bar{\psi}$ into one of its generating Hamiltonian functions $\mathcal{H}(\bar{\psi}) : \mathbb{R} \times \mathbb{R}^{2d} \rightarrow \mathbb{R}^{2d}$, all of which differ by a function of the time variable t . In this way, the Hamiltonian of the network $\mathcal{H}(\bar{\psi})$ corresponds to $H_t^{L:1}$ defined as in Equation (6).

2.3 Training the SympFlow

In Section 4 we apply SympFlow to approximate the flow map of an autonomous Hamiltonian system of the form $\dot{x}(t) = \mathbf{J}\nabla H(x(t)) \in \mathbb{R}^{2d}$ in both *supervised* and *unsupervised* settings. In what follows we describe the relevant training objectives for both of these. In all the experiments below, we assume there exists a forward invariant compact subset $\Omega \subset \mathbb{R}^{2d}$, meaning that if $x_0 \in \Omega$ also $\phi_{H, t}(x_0) \in \Omega$ for every $t \geq 0$. This forward-invariance assumption allows us to make predictions for any time $t \geq 0$, once we are able to make them sufficiently accurate for initial conditions in Ω , and time instants in a compact interval $[0, \Delta t]$. More explicitly, let us consider a function $\bar{\psi} : [0, \Delta t] \times \Omega \rightarrow \Omega$ providing an accurate approximation of the exact flow $\phi_{H, t}$ for $t \in [0, \Delta t]$. We can extend $\bar{\psi}$ to $[0, +\infty) \times \Omega \rightarrow \Omega$ defined as

$$\psi(t, x_0) := \bar{\psi}_{t-\Delta t \lfloor t/\Delta t \rfloor} \circ (\bar{\psi}_{\Delta t})^{\lfloor t/\Delta t \rfloor}(x_0), \quad (7)$$

where we recall that $\bar{\psi}_t(x_0) = \bar{\psi}(t, x_0)$,

$$(\bar{\psi}_1)^{\lfloor t/\Delta t \rfloor} = \underbrace{\bar{\psi}_1 \circ \dots \circ \bar{\psi}_1}_{\lfloor t/\Delta t \rfloor \text{ times}}$$

and $\lfloor t/\Delta t \rfloor$ is the largest integer smaller or equal than $t/\Delta t \in [0, +\infty)$. The map $\psi(t, x_0)$ provides an approximation of $\phi_{H, t}(x_0)$ for every $t \geq 0$ and $x_0 \in \Omega$.

Regression loss term In the *supervised* setting, we aim to approximate the flow map $\phi_{H, t} : \Omega \rightarrow \Omega$ of an unknown Hamiltonian system with Hamiltonian function H . For this supervised problem, we suppose to have access to observed trajectories, all collected in the set

$$\{y_m^n = \phi_{H, t_m^n}(x_0^n) + \varepsilon_m^n : n = 1, \dots, N, m = 1, \dots, M\},$$

where ε_m^n is a perturbation due to noise or discretization errors, $x_0^n \in \Omega \subset \mathbb{R}^{2d}$, and $t_m^n \in [0, \Delta t]$. The training process is thus purely based on data, and we minimize the mean squared error

$$\mathcal{L}(\bar{\psi}) = \frac{1}{NM} \sum_{n=1}^N \sum_{m=1}^M \|\psi(t_m^n, x_0^n) - y_m^n\|_2^2, \quad (8)$$

where $\bar{\psi} : [0, \Delta t] \times \mathbb{R}^{2d} \rightarrow \mathbb{R}^{2d}$ can be a SympFlow or an MLP. Both networks take time as an input, allowing us to deal with non-uniformly sampled trajectory data. An example dataset for the simple harmonic oscillator can be seen in Figure 2.

In the *unsupervised* setting, based on the analysis in Section 2.2, we consider a loss function composed of two terms, namely a residual loss term and a Hamiltonian matching term, to find the weights of a SympFlow.

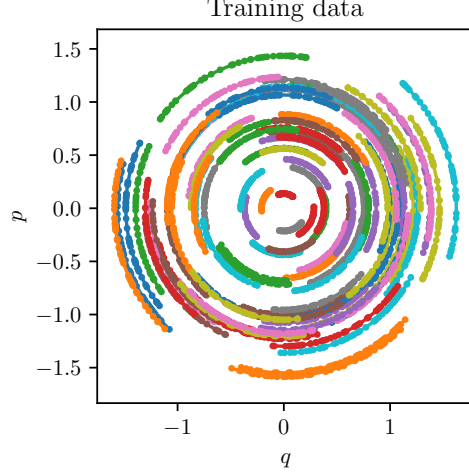


Figure 2: Training data with $N = 100$ initial conditions, $M = 50$ sampling times for each of them, and no noise, i.e., $\varepsilon_m^n = 0$ for every n and m .

Residual loss term The first term is typical for operator learning tasks, see [58, e.g.], and is defined as

$$\mathcal{L}_1(\bar{\psi}) = \frac{1}{N} \sum_{i=1}^N \left\| \left. \frac{d}{dt} \bar{\psi}(t, x_0^i) \right|_{t=t_i} - \mathbf{J} \nabla H(\bar{\psi}(t_i, x_0^i)) \right\|_2^2, \quad (9)$$

where $x_0^i \in \Omega$ and $t_i \in [0, \Delta t]$ for every $i = 1, \dots, N$. For this, $\bar{\psi} : [0, \Delta t] \times \mathbb{R}^{2d} \rightarrow \mathbb{R}^{2d}$ can be a SympFlow or an MLP.

Hamiltonian Matching term The Hamiltonian structure of the SympFlow gives us a natural way to regularize the training phase. To that end, we use a Hamiltonian matching approach [7] that introduces an additional term in the loss function, defined as

$$\mathcal{L}_2(\bar{\psi}) = \frac{1}{M} \sum_{i=1}^M (\mathcal{H}(\bar{\psi})(t_i, x^i) - H(x^i))^2, \quad (10)$$

where $x^i \in \Omega$ and $t_i \in [0, \Delta t]$ for every $i = 1, \dots, N$.

In the experimental analysis, we will compare SympFlow to an unconstrained multi-layer perceptron (MLP). To have an unbiased comparison, the MLP is trained with the residual loss function to which we add the alternative energy regularization term

$$\tilde{\mathcal{L}}_2(\bar{\psi}) = \frac{1}{M} \sum_{i=1}^m (H(\bar{\psi}(t^i, x^i)) - H(x^i))^2, \quad (11)$$

where $t^i \in [0, \Delta t]$, $x^i \in \Omega$, and $\bar{\psi} : [0, \Delta t] \times \Omega \rightarrow \Omega$ is the MLP. This regularization term informs this unconstrained network that the Hamiltonian energy should be conserved. We remark that Equation (11) differs from Equation (10) in that we do not have a modified Hamiltonian $\mathcal{H}(\bar{\psi})$ in the MLP case, and hence we only promote the conservation of the actual Hamiltonian energy H .

The loss function is then given by

$$\mathcal{L}(\bar{\psi}) = \mathcal{L}_1(\bar{\psi}) + \mathcal{L}_2(\bar{\psi}), \quad (12)$$

with \mathcal{L}_1 and \mathcal{L}_2 defined as in Equation (9) and Equation (10). For the MLP, we replace \mathcal{L}_2 with $\tilde{\mathcal{L}}_2$. Notice that $\mathcal{H}(\bar{\psi})$ is the exact Hamiltonian behind the SympFlow ψ , and the loss $\mathcal{L}_2(\bar{\psi})$ provides a comparison between the exact flow $\phi_{H,t}$ and the SympFlow via zeroth-order information, i.e., based on the exact energies behind those maps. Importantly, the \mathcal{L}_2 term allows us to perform a *backward error analysis*—while SympFlow does not generally solve the ODE under consideration, it solves a time-dependent Hamiltonian ODE, for a Hamiltonian which is driven towards H during the training process. The fact that $\mathcal{H}(\bar{\psi})$ is time-dependent implies that the flow $\bar{\psi}$ does not conserve \mathcal{H} , as it is expected for non-autonomous Hamiltonian systems. However, if (10) is small enough, the Hamiltonian $\mathcal{H}(\bar{\psi})$ will not be strongly dependent on time, hence leading to an almost conservation of H by the SympFlow. We further expand on this aspect below.

3 Theoretical analysis of the SympFlow

This section provides a theoretical a-posteriori analysis of a SympFlow approximating the target map $\phi_{H,t}$. This result relies on the assumption that the map $\phi_{H,t}$ can be accurately approximated for $t \in [0, \Delta t]$ by a SympFlow. This is possible since SympFlows are universal approximators in the space of Hamiltonian flows. We state this result in Theorem 1, and prove it in Appendix D.

Theorem 1 (Universal approximation theorem for SympFlow). *Let $H : \mathbb{R} \times \Omega \rightarrow \mathbb{R}$, $\Omega \subset \mathbb{R}^{2d}$ compact, be a continuously differentiable function. For any $\varepsilon > 0$, there is a SympFlow $\bar{\psi}_t$ such that*

$$\sup_{\substack{t \in [0, \Delta t] \\ x \in \Omega}} \|\bar{\psi}_t(x) - \phi_{H,t}(x)\|_\infty < \varepsilon.$$

Outline of the proof of Theorem 1. The proof is based on the following steps:

1. Approximate the flow $\phi_{H,t}$ with the flow $\phi_{\tilde{H},t}$ of a polynomial Hamiltonian system with Hamiltonian $\tilde{H} : \mathbb{R} \times \Omega \rightarrow \mathbb{R}$.
2. Split the exact polynomial flow $\phi_{\tilde{H},t}$ into sufficiently many N substeps of size t/N .
3. Approximate to $\mathcal{O}(1/N^2)$ each of the flows defining the N substeps with flows of separable Hamiltonian systems.
4. Approximate the flows of separable Hamiltonian systems of the previous point with SympFlows.
5. Combine the approximations and use the fact that the composition of SympFlows is again a SympFlow.

The details can be found in Appendix D. □

Remark 1. *For the a-posteriori analysis, we assume that there is a compact subset $\Omega \subset \mathbb{R}^{2d}$ which is forward invariant both for the flow $\phi_{H,t}$ we are approximating and for the network $\bar{\psi}_t$. More explicitly, we assume that $\bar{\psi}_t(x_0) \in \Omega$ for every $x_0 \in \Omega$ and $t \in [0, \Delta t]$, and $\phi_{H,t}(x_0) \in \Omega$ for every $x_0 \in \Omega$ and $t \geq 0$.*

Based on the time extension provided in Equation (7) and Remark 1, one can obtain a function which accurately approximates a target flow map $\phi_{H,t} : \Omega \rightarrow \Omega$ for every time $t \geq 0$. This time extension is again the composition of Hamiltonian flows, hence possessing an underlying time-dependent Hamiltonian. For a fixed time, $t \geq 0$, the function in Equation (7) satisfies

$$\begin{aligned} \frac{d}{dt} \psi(t, x_0) &= \frac{d}{dt} \left(\bar{\psi}_{t-\Delta t \lfloor t/\Delta t \rfloor} \circ (\bar{\psi}_{\Delta t})^{\lfloor t/\Delta t \rfloor} \right) (x_0) \\ &= \mathbf{J}\nabla (\mathcal{H}(\bar{\psi})) (t - \Delta t \lfloor t/\Delta t \rfloor, \psi(t, x_0)), \end{aligned} \quad (13)$$

almost everywhere. We provide details about the derivation of Equation (13) in Appendix B. From Equation (13), we see that the long-time extension of a SympFlow is again the solution of a non-autonomous Hamiltonian system with time-dependent Hamiltonian function $\mathcal{H}(\psi) : [0, +\infty) \times \mathbb{R}^{2d} \rightarrow \mathbb{R}^{2d}$ defined as

$$\mathcal{H}(\psi)(t, x) = \mathcal{H}(\bar{\psi})(t - \Delta t \lfloor t/\Delta t \rfloor, x). \quad (14)$$

Therefore, the Hamiltonian in Equation (14) is piecewise continuous, and this is because ψ is not differentiable at the time instants $t_k = k\Delta t$, $k \in \mathbb{N}$.

Theorem 2 (A-posteriori error estimate). *Let $\bar{\psi} : [0, \Delta t] \times \Omega \rightarrow \Omega$ be a SympFlow. Let us assume that for every $x \in \Omega$ and $t \in [0, \Delta t]$*

$$|\mathcal{H}(\bar{\psi})(t, x) - H(x)| \leq \varepsilon_1, \quad (15)$$

and also

$$\left\| \frac{d}{dt} \bar{\psi}_t(x) - \mathbf{J}\nabla H(\bar{\psi}_t(x)) \right\|_2 \leq \varepsilon_2 \quad (16)$$

for a pair of values $\varepsilon_1, \varepsilon_2 > 0$. Then there exist $c_1, c_2 > 0$ such that for every $t \geq 0$ and $x \in \Omega$

$$|\mathcal{H}(\psi)(0, x) - \mathcal{H}(\psi)(t, \psi_t(x))| \leq c_1 \varepsilon_1 t, \quad (17)$$

$$|H(x) - H(\psi_t(x))| \leq c_2 (\varepsilon_1 + \varepsilon_2 t), \quad (18)$$

where ψ is defined as in Equation (7), and $\mathcal{H}(\psi)$ as in Equation (14).

We prove Theorem 2 in Appendix C. We remark that Equation (18) can be obtained with similar techniques for any neural network satisfying Equation (16), while Equation (17) only in the case one has a `SympFlow` and some a-posteriori bound as in Equation (15). Furthermore, we also point out that the assumptions in Equation (15) and Equation (16) correspond to saying that the loss function in Equation (12) is smaller than a specific constant, hence why this is an a-posteriori error estimate.

4 Numerical Experiments

In this section, we demonstrate the effectiveness of our proposed architecture, `SympFlow`, in two tasks: (i) solving the equations of motion of a given time-independent Hamiltonian system, and (ii) approximating the solution map of an unknown Hamiltonian system based on data.

The proposed experimental analysis compares the results obtained with `SympFlow` and an unconstrained neural network, which we will refer to as MLP. We provide some details on the network architectures in Appendix E.

We consider three test problems: the simple harmonic oscillator, the damped harmonic oscillator, and the Hénon–Heiles system. Details on these Hamiltonian systems are provided in Section 4.1, Section 4.2, and Section 4.3. For each test problem, we first consider the unsupervised task of solving the equations of motion. We then move on to consider the supervised task of estimating the flow based on irregular trajectory samples. The training process for these experiments follows the steps presented in Section 2.3.

For the three systems, we show the effectiveness of the proposed methodology by presenting quantitative and qualitative comparisons between the various models. For the simple harmonic oscillator, we also analyze the impact of noise, the value of N , and the value of M on the approximation accuracy. In this case, we will model the noise affecting trajectories with random normal variables of zero mean and standard deviation ε , where ε is used to quantify the noise intensity. Our trajectory data is synthetically generated with a Runge–Kutta (5, 4) integrator with tight tolerance. Consequently, the trajectories are also affected by discretization error.

As we will see across all the simulations, `SympFlow` leads to considerably improved long-time energy behavior compared to MLP.

4.1 One dimensional Simple Harmonic Oscillator

The one-dimensional simple harmonic oscillator is a foundational problem in both physics and engineering. Studying its dynamics offers valuable insights into the behavior of classical mechanical systems as well as quantum systems. The simple harmonic oscillator equations of motion are analytically solvable, making it an ideal benchmark for evaluating the accuracy and performance of both classical and neural network-based solvers.

Without loss of generality, we consider a spring with a spring constant k , where one end is attached to a point mass m and the other end is fixed in place. The Hamiltonian of this system is given by

$$H(q, p) = \frac{1}{2m}p^2 + \frac{k}{2}q^2, \quad (19)$$

where q, p are the position and momentum of the point mass. In our experiments, we fix the recovery constant to $k = 1$ and the mass to $m = 1$. The equations of motion of this system write

$$\dot{q} = \frac{\partial H}{\partial p} = \frac{p}{m}, \quad \dot{p} = -\frac{\partial H}{\partial q} = -kq. \quad (20)$$

We now move to the two experimental settings we consider for this system. All the experiments fix $\Delta t = 1$ and $\Omega = [-1.2, 1.2]^2 \subset \mathbb{R}^2$.

4.1.1 Unsupervised experiments

In this section, we compare the `SympFlow` architecture with an unconstrained MLP on solving the equations of motion in Equation (20). We train the `SympFlow` in three different ways, aiming to identify the impact of the two terms in the loss function, see Equation (12). The MLP is instead always trained with the regularization term in Equation (11). In the figures, the term regularization refers to the addition of the Hamiltonian matching term in Equation (10). When a `SympFlow` is trained with Hamiltonian regularization, it means it is trained to minimize the loss in Equation (12). If there is no such regularization, it means that we only train with the residual-based loss function in Equation (9). We also consider a mixed training procedure, which consists of a first training phase with Hamiltonian regularization, and a later fine-tuning of the weights by training the model for a few more epochs without Hamiltonian matching.

Figure 3 reports the results obtained with these four training configurations. We see that the SympFlow architecture consistently outperforms the unconstrained MLP in predicting the correct qualitative behavior of the solution. This is evident both looking at the reproduced orbit, which are all associated to the initial condition $(q_0, p_0) = (1, 0)$, but also in the long-time energy behavior. We remark that the orbit of $(1, 0)$ is wholly contained in Ω , so the networks are expected to approximate it reliably. The second column in Figure 3 shows the variation of the true Hamiltonian energy in Equation (19) along the network-produced solutions. Even though we extrapolate over the long integration time $[0, 1000]$, the SympFlow outperforms the MLP regardless of how it has been trained. This is a consequence of the symplectic nature of the network. In this experiment, it is unclear whether the three different considered training procedures for the SympFlow have a significant impact. We explore this further in the other two test problems.

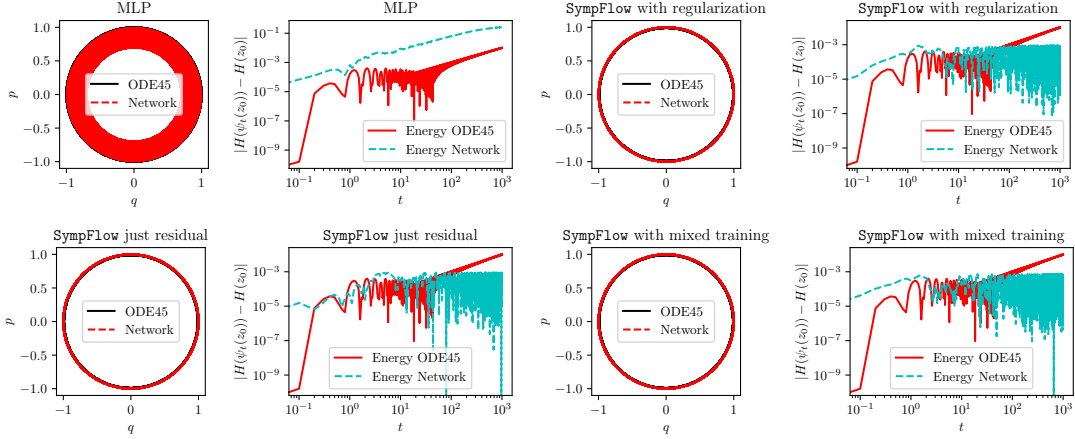


Figure 3: **Unsupervised experiment — Simple Harmonic Oscillator:** Comparison of the results obtained with predictions up to time $T = 1000$ and $\Delta t = 1$.

4.1.2 Supervised experiments

We now move to the supervised experiments, where we recall that the models are trained based on the mean squared error loss function in Equation (8). We first show in Figure 4 the obtained results with $N = 100$ initial conditions, each sampled at possibly different $M = 50$ time instants. In this case, we assume there is no noise, i.e., $\varepsilon = 0$. The results in Figure 4 show a similar pattern to the unsupervised experiments, where the SympFlow outperforms the MLP over long time simulations. Comparing this figure with Figure 3, we notice that the unsupervised case leads to a smaller energy variation than the supervised one for SympFlow predictions. This difference is expected since the unsupervised experiment, even though it does not rely on trajectory data, relies on the knowledge of the Hamiltonian system one is trying to solve, hence having access to the true Hamiltonian function while training the network.

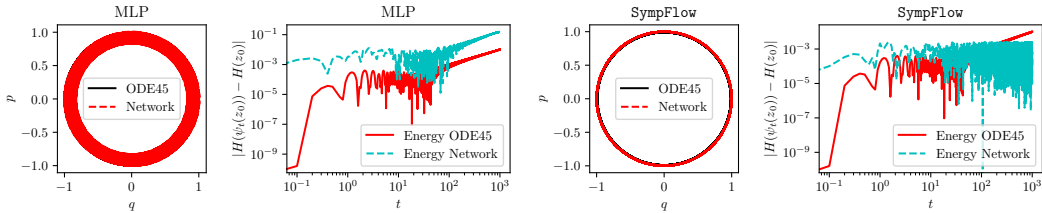


Figure 4: **Supervised experiment — Simple Harmonic Oscillator:** Comparison of the MLP and the SympFlow trained with a dataset of parameters $N = 100$, $M = 50$, and $\varepsilon = 0$.

We now evaluate the impact of the three parameters N , M , and ε on the performance of SympFlow and MLP. We denote with $\psi : \mathbb{R} \times \mathbb{R}^{2d} \rightarrow \mathbb{R}^{2d}$ the extension of the network $\bar{\psi}$ over the real line, defined as in Equation (7). To quantitatively evaluate the results and compare the models, we consider the average relative error

$$\frac{1}{I} \sum_{i=1}^I \frac{\|\psi(k\Delta t, x_i^0) - \phi_{H,k\Delta t}(x_i^0)\|_2}{\|\phi_{H,k\Delta t}(x_i^0)\|_2}, \quad k = 1, 10, 100$$

over $I = 100$ randomly sampled initial conditions in Ω . We remark that even though the quantity above is expressed using the exact flow map $\phi_{H,t}$, in practice, we replace it with a reference numerical solution obtained using a Runge–Kutta (5, 4) integrator with tight tolerance. We also test the average relative Hamiltonian energy variation

$$\frac{1}{I} \sum_{i=1}^I \frac{|H(\psi(k\Delta t, x_i^0)) - H(x_i^0)|}{|H(x_i^0)|}, \quad k = 1, 10, 100.$$

We collect the values of these two metrics in Figure 5. Each of the three subfigures lets one of the three parameters vary and fixes the other two. We now discuss some outcomes from this experimental analysis:

- The energy variation for SympFlow is always smaller than for MLP. Furthermore, this gap widens as time progresses.
- The relative error at $100\Delta t$ for the two models is comparable in all of the configurations. This is expected for two reasons:
 1. The simple harmonic oscillator does not have complicated dynamics, so we get accurate results with both models. We will later demonstrate how the more complex dynamics of the Hénon–Heiles system posed a significant challenge for the MLP, further highlighting the strengths of SympFlow.
 2. The fact that SympFlow is symplectic does not ensure improved quantitative long-time behavior, but qualitative. This is also why one would not expect a symplectic time integrator to be more accurate than a classical one. However, as for the energy behavior above, the qualitative properties of the produced solutions are considerably improved.
- Even in the presence of noise, the SympFlow outperforms MLP. This can be seen by looking at the error at time Δt for different values of ε in Figure 5c. The symplectic constraint on SympFlow prevents it from overfitting the data and learning the noise.
- The MLP looks to benefit from additional data much more than SympFlow. This can be seen in the relative errors and energy variations as N and M increase. This can be interpreted as a consequence of the fact that MLP has no encoded structure, and to infer the correct behavior, it needs a considerable amount of data.

4.2 Modelling Dissipation: Damped Harmonic Oscillator

Real-world dynamical systems often dissipate energy to their surroundings through mechanisms such as heat, friction, or radiative losses. These processes reduce the energy of the system until it reaches equilibrium. To accurately capture the dynamics of dissipative physical systems, it is critical to account for those effects within their equations of motion. To apply our approach to non-conservative systems, we adopt the formulation introduced in [23], which allows to express their dynamics as conservative systems in a phase space having doubled dimension compared to the physical space. This formalism enables to accommodate dissipation while retaining key features of the Hamiltonian dynamics, such as symplecticity, and hence apply SympFlow in a meaningful way. For more details on this formalism, see Appendix A. In this formulation, the degrees of freedom are doubled, and a point in this augmented space is given by $z_{a,b} := (q_a, q_b, \pi_a, \pi_b) \in \mathbb{R}^{4d}$, where π_a and π_b are the so-called non-conservative momenta. The Hamiltonian of the augmented system is given by the function

$$A(q_a, q_b, \pi_a, \pi_b) = H(q_a, \pi_a) - H(q_b, \pi_b) - K(q_a, q_b, \pi_a, \pi_b), \quad (21)$$

where $H : \mathbb{R}^{2d} \rightarrow \mathbb{R}$ is the Hamiltonian of the system, and $K : \mathbb{R}^{4d} \rightarrow \mathbb{R}$ is an interaction term modeling the action of the non-conservative forces. In our experiments, the function K takes the form [55, 24]

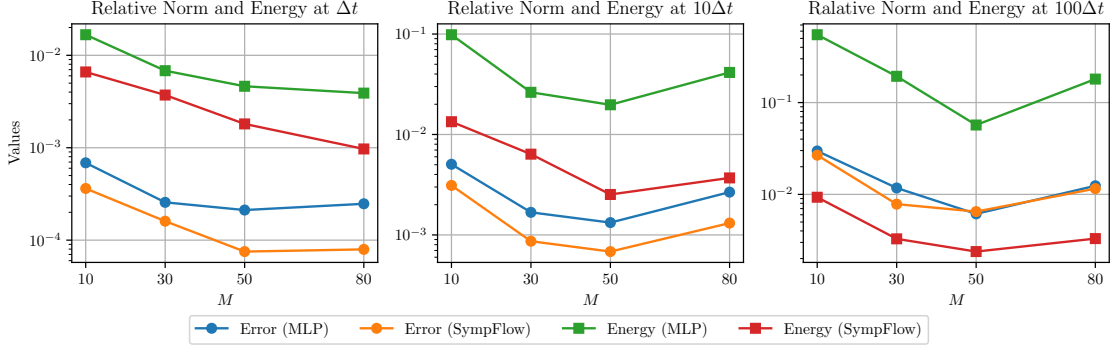
$$K(q_a, q_b, \pi_a, \pi_b) = -\frac{\lambda}{2}(\dot{q}_a + \dot{q}_b)(q_a - q_b),$$

giving rise to a damped harmonic oscillator. Although a trajectory described by the original phase-space variables, $(q(t), p(t))$, does not follow a conservative dynamics, the trajectory described in the augmented space, is indeed conservative. Hence, in the augmented space, the map $(t, z_{a,b}(0)) \mapsto z_{a,b}(t)$ is symplectic and the equations of motion can be recast in a symplectic form:

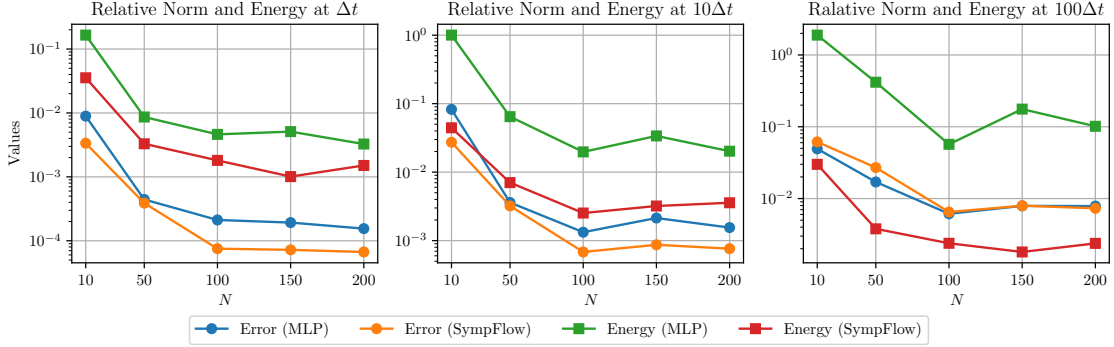
$$\dot{z}_{a,b}(t) = \mathbf{J}\nabla A(z_{a,b}(t)), \quad (22)$$

with the corresponding equations of motion given by:

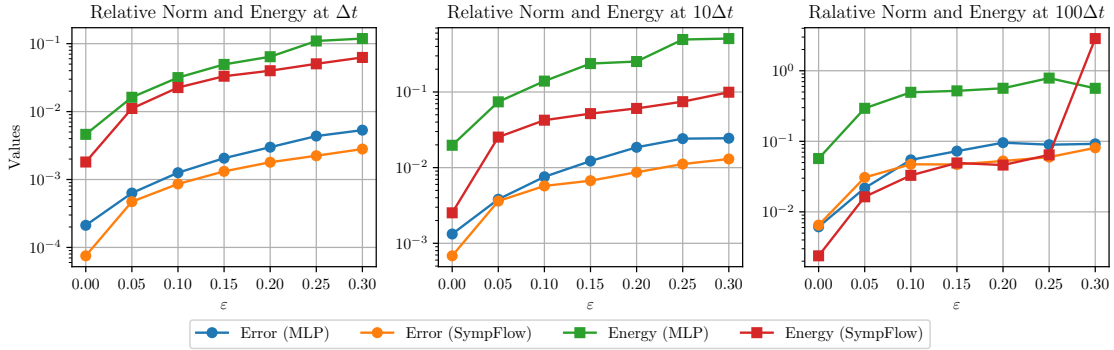
$$\begin{aligned} \dot{q} &= \frac{\partial H}{\partial p} - \left[\frac{\partial K}{\partial \dot{q}_I} \right]_{\text{PL}} \\ \dot{p} &= -\frac{\partial H}{\partial q} + \left[\frac{\partial K}{\partial \dot{q}_I} \right]_{\text{PL}}, \end{aligned} \quad (23)$$



(a) Relative ℓ^2 -norms of the error and the energy variations at times $\Delta t, 10\Delta t, 100\Delta t$ for a fixed $N = 100$ and $\varepsilon = 0$.



(b) Relative ℓ^2 -norms of the error and the energy variations at times $\Delta t, 10\Delta t, 100\Delta t$ for a fixed $M = 50$ and $\varepsilon = 0$.



(c) Relative ℓ^2 -norms of the error and the energy variations at times $\Delta t, 10\Delta t, 100\Delta t$ for a fixed $N = 100$ and $M = 50$.

Figure 5: **Supervised experiment — Simple Harmonic Oscillator:** Impact of the parameters N , M , and ε on the training procedure.

where PL stands for physical limit and corresponds to the restriction to the linear subspace

$$\{(q_a, q_b, \pi_a, \pi_b) \in \mathbb{R}^{4d} : q_a = q_b, \text{ and } \pi_a = -\pi_b\},$$

see Appendix A.

4.2.1 Unsupervised experiments

Similarly to the harmonic oscillator example in Section 4.1, we solve the system's equations of motion with the SympFlow architecture and with an unconstrained MLP. The MLP is again regularized by the additional loss term in Equation (11). In this section, we experiment training SympFlow with: i) Hamiltonian regularization Equation (12) and b) residual-based loss function Equation (9). We train both networks for 50,000 epochs, setting $\Delta t = 1$. Figure 6 show the damped harmonic oscillator solutions for both MLP and SympFlow, and for increasing values of the damping

constant λ . We can see that both networks are able to capture the dissipative dynamics of the system for the different values of λ . This result is further supported by the left subfigure of Figure 9, where we also notice that adding an energy regularization term does not seem to improve SympFlow’s overall performance.

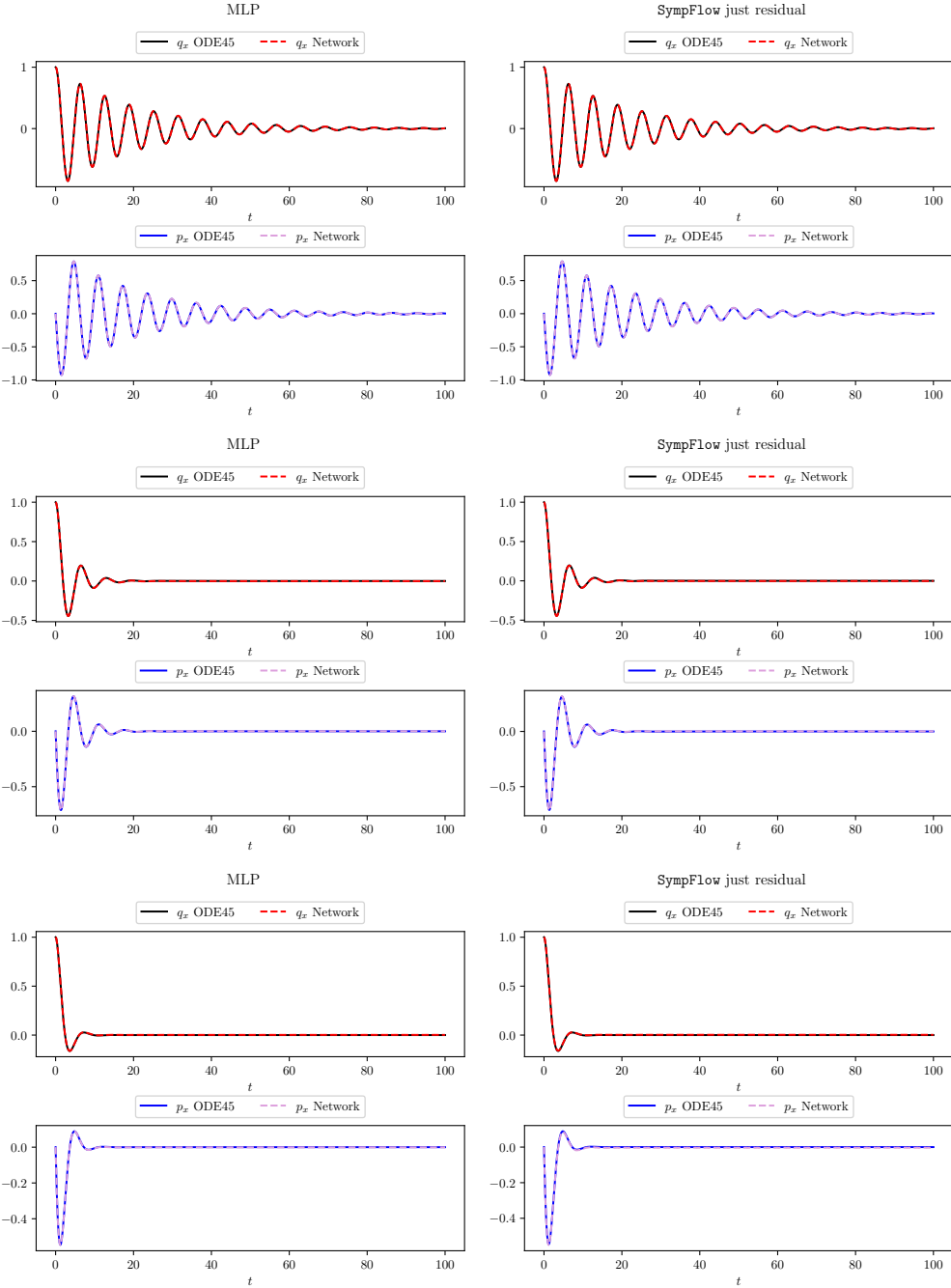


Figure 6: Damped harmonic oscillator solutions, where q_x is the 1D position and p_x is the (conservative) 1D momentum of the oscillator’s mass for different values of the damping constant λ , Appendix A. **Top:** $\lambda = 0.1$, **middle:** $\lambda = 0.5$, and **bottom:** $\lambda = 1$.

4.2.2 Supervised experiments

In this section we compare the performance of the MLP network and SympFlow, trained with $N = 50$ initial conditions and $M = 10$ time samples for each of them. Figure 7, Figure 8, and Figure 9 show that SympFlow outperforms the MLP

network when the dynamics of the system is more complex (case $\lambda = 0.1$) and presents oscillations with decreasing amplitude, whereas for solutions with less complex behavior both methods seem to perform similarly well.

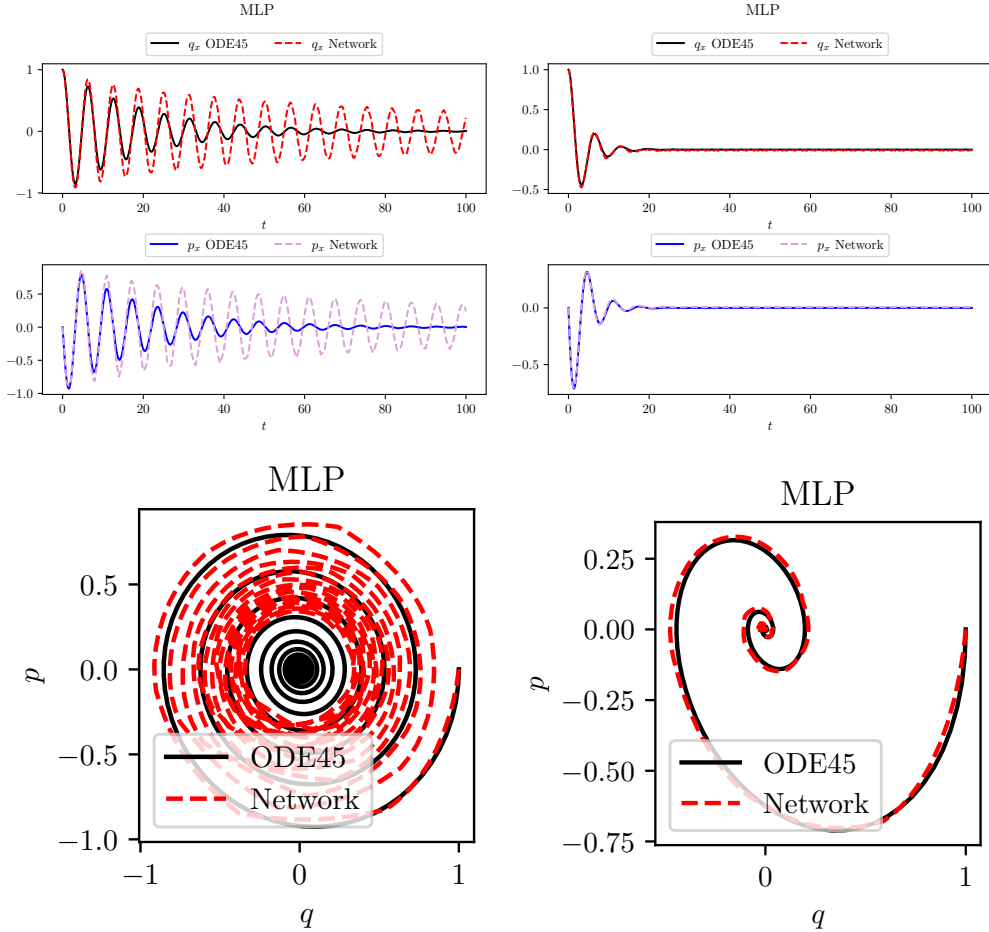


Figure 7: **MLP Supervised experiment — Damped Harmonic Oscillator:** Trained with $N = 50$, $M = 10$, and no noise, $\varepsilon = 0$.

4.3 Hénon–Heiles system

The Hénon–Heiles system is a model for studying non-linear dynamics, chaos, and the transition from regular to chaotic motion in physics. Initially developed to understand the motion of a star in a galactic potential, the system has since become a paradigmatic example in the study of chaos theory. The Hénon–Heiles system is a Hamiltonian system based on the Hamiltonian function [28, Section I.3]

$$H(q, p) = \frac{1}{2}(p_x^2 + p_y^2) + \frac{1}{2}(q_x^2 + q_y^2) + q_x^2 q_y - \frac{q_y^3}{3}, \quad q = (q_x, q_y), p = (p_x, p_y) \in \mathbb{R}^2. \quad (24)$$

The equations of motion for this system write

$$\dot{q}_x = p_x, \quad \dot{q}_y = p_y, \quad \dot{p}_x = -q_x - 2q_x q_y, \quad \dot{p}_y = -q_y - (q_x^2 - q_y^2). \quad (25)$$

The equations of motion in Equation (25) provide a considerable challenge to numerical integrators and network-based simulations since they exhibit chaotic behavior corresponding to specific energy levels. Due to the chaotic nature of the system, it is unreasonable to expect a long-term agreement of the approximation with the exact solution. However, for chaotic systems, one would like to capture the correct global behavior of the trajectories. A common strategy to test this is to consider a two-dimensional Poincaré section and compare the obtained results for different methods. We proceed in this way to compare SympFlow with an MLP. To that end, we start by considering the Poincaré section corresponding to the linear subspace

$$\mathcal{S} = \{(0, q_y, p_x, p_y) : q_y, p_x, p_y \in \mathbb{R}\}, \quad (26)$$

Symplectic Neural Flows

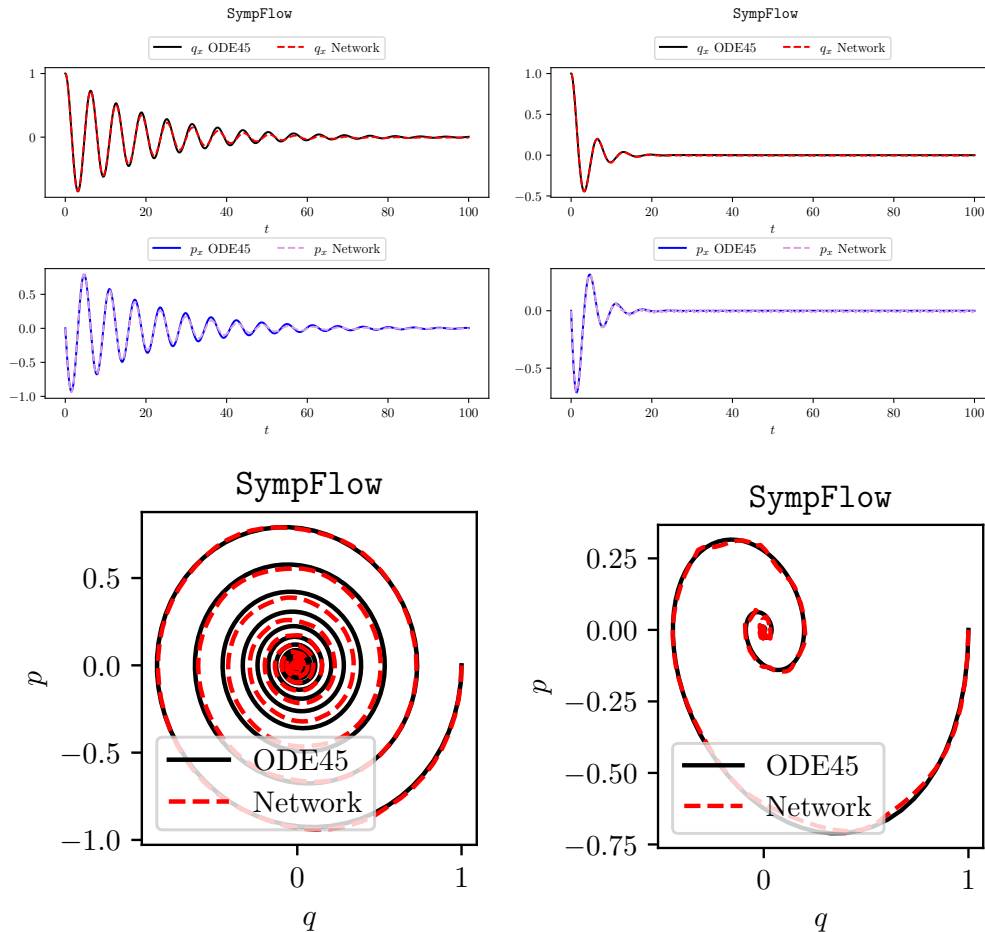


Figure 8: Symplectic Neural Flows supervised experiment without regularization — Damped Harmonic Oscillator: Trained with $N = 50$, $M = 10$, and no noise, $\varepsilon = 0$. procedure.

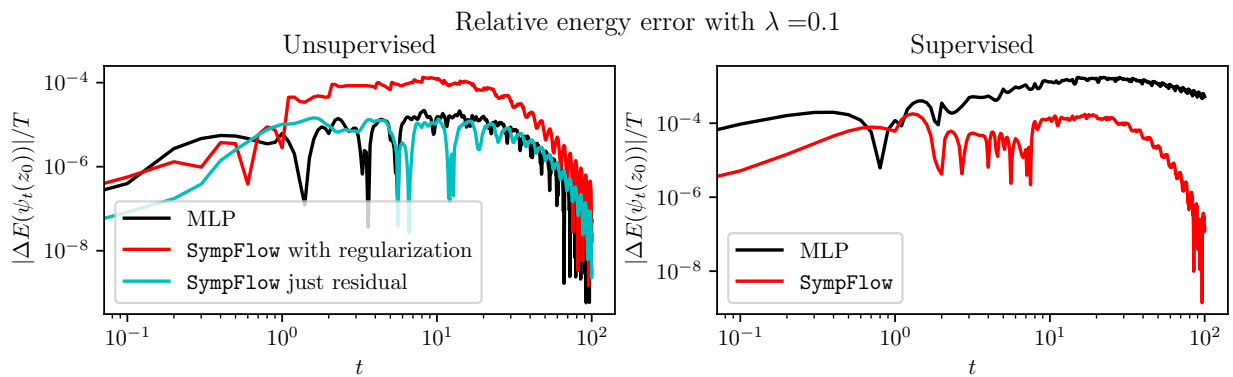


Figure 9: Comparison of the damped harmonic oscillator relative energy, normalised over the integration time, for unsupervised (left) and supervised (right) experiments. In the unsupervised case, both the MLP and SympFlow. In the supervised case, the solutions have been computed with $N = 50$ initial conditions and $M = 10$ sampling points. In this setting, with fewer initial conditions, SympFlow outperforms MLP.

and we will provide a planar representation, in the variables (q_y, p_y) , of the intersection of the trajectories with the section \mathcal{S} . For a definition of the notion of attractor, and Poincaré sections, see [51].

We now move to the two experimental settings we consider for this system. All the experiments fix $\Delta t = 1$ and $\Omega = [-1, 1]^4 \subset \mathbb{R}^4$. Some of these initial conditions correspond to energy levels leading to chaotic dynamics. However, since the training process only relies on the short integration interval $[0, 1]$, this does not seem to negatively affect the quality of the recovered models.

4.3.1 Unsupervised experiments

As for the previous two test problems, we consider the unsupervised problem of solving the differential equations in Equation (25) for arbitrary initial conditions in $\Omega \subset \mathbb{R}^4$, and for time instants in $[0, \Delta t]$. The plots consider the initial condition $(0.3, -0.3, 0.3, 0)$, leading to initial energy $H_0 = 0.13$, corresponding to chaotic dynamics. We collect in Figure 10 the experiments with the three training regimes for SympFlow and with an MLP, again regularized by Equation (11). We see that SympFlow leads to better long-term energy behavior, and that the mixed training regime leads to slightly improved results. We also plot the Poincaré cuts associated with the section in Equation (26). A reference cut obtained with Runge–Kutta (5, 4) can be found in Appendix F. The SympFlows lead to much more qualitatively accurate solutions, given that the obtained cuts resemble the expected behavior. Appendix F also collects the plots of the solution curves obtained with this initial condition for the four trained models.

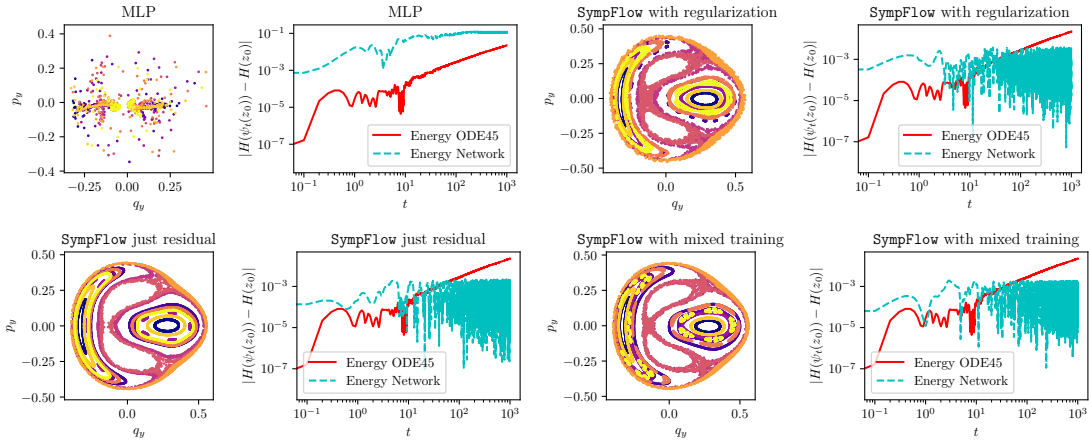


Figure 10: **Unsupervised experiment — Hénon–Heiles:** Comparison of the Poincaré sections and the energy behavior up to time $T = 1000$.

4.3.2 Supervised experiments

For the supervised experiment, we notice a pretty similar situation as in the unsupervised one, as can be seen in Figure 11. In this setup, it is also very hard to train the MLP model, as can be seen from the produced solution curves in Figure 13 of Appendix F. Once more, SympFlow demonstrates the ability to capture the correct global qualitative behavior of the solutions as we can see in both the energy plot and the Poincaré cuts in Figure 11.

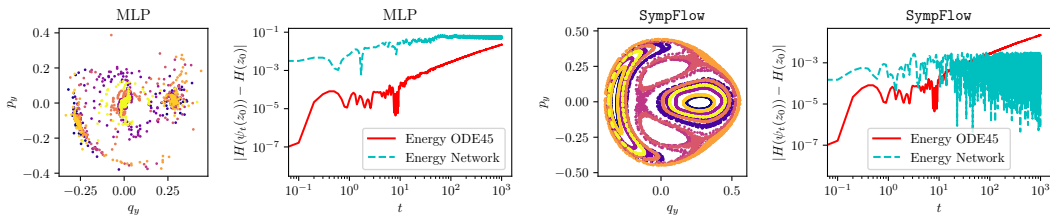


Figure 11: **Supervised experiment — Hénon–Heiles:** Comparison of the MLP and the SympFlow trained with a dataset of parameters $N = 100$, $M = 50$, and $\varepsilon = 0$. We show the energy plots for the time interval $[0, 1000]$, and also the Poincaré sections obtained with the two different networks.

5 Conclusions and further work

In this work we presented SympFlow, a symplectic neural flow able to provide accurate and reliable long-term solutions for generic Hamiltonian systems. We have shown that SympFlow is a universal approximator and it can be applied to (i) approximately solve the equations of motion of Hamiltonian systems and (ii) approximate the flow map of unknown Hamiltonian system based on trajectory data. Because of its structure, SympFlow admits an underlying Hamiltonian which could also be used to study an approximated physical model, a task which has previously been studied in the scientific machine learning literature [3, 26]. Potentially, both SympFlow functionalities, (i)-(ii), can be combined to model complex physical systems. We have also demonstrated the advantages of SympFlow over an unconstrained MLP in several experimental tasks, including a chaotic system and a non-conservative system.

The numerical experiments, show that the performance of the SympFlow is equal or superior to an MLP network for unsupervised tasks. For supervised tasks, however, SympFlow outperforms MLP to approximate complex solution, in particular when the number of initial conditions and time samples are significantly reduced, hence, highlighting the data efficiency of SympFlow.

There are several natural ways to extend this research. From the theoretical point of view, it would be interesting to further explore the energy behavior of the SympFlow since we experimentally observe a better error growth than the one in Theorem 2. We will also expand the applicability of SympFlow to higher-dimensional dynamical systems, such as spatially semi-discretized PDEs. To do so, the main effort will be in improving the computational efficiency of the SympFlow layers, which currently rely on automatic differentiation which can be costly for higher dimensional problems.

Acknowledgements

The authors would like to thank Georg Maierhofer for useful discussions. DM acknowledges support from a grant from the Simons Foundation, the EPSRC Programme Grant on the Mathematics of Deep Learning (Maths4DL), and the Norwegian University of Science and Technology. CBS acknowledges support from the Philip Leverhulme Prize, UK, the Royal Society Wolfson Fellowship, UK, the EPSRC advanced career fellowship, UK EP/V029428/1, EPSRC grants EP/S026045/1 and EP/T003553/1, EP/N014588/1, EP/T017961/1, the Wellcome Innovator Awards, UK 215733/Z/19/Z and 221633/Z/20/Z, the European Union Horizon 2020 research and innovation programme under the Marie Skłodowska-Curie grant agreement No.777826 NoMADS, the Cantab Capital Institute for the Mathematics of Information, UK and the Alan Turing Institute, UK. FS acknowledges support from the EPSRC advanced career fellowship EP/V029428/1. PC thanks the Alan Turing Institute for sponsoring her Daphne Jackson Fellowship. ZS acknowledges support from the Cantab Capital Institute for the Mathematics of Information and the Trinity Henry Barlow Scholarship scheme.

References

- [1] V. I. ARNOLD, *Ordinary Differential Equations*, MIT Press, Cambridge, Mass., 8. print ed., 1991.
- [2] S. ARORA, A. BIHLO, AND F. VALIQUETTE, *Invariant physics-informed neural networks for ordinary differential equations*, 2024, <https://arxiv.org/abs/2310.17053>. arXiv:2310.17053.
- [3] T. BERTALAN, F. DIETRICH, I. MEZIĆ, AND I. G. KEVREKIDIS, *On learning Hamiltonian systems from data*, *Chaos: An Interdisciplinary Journal of Nonlinear Science*, 29 (2019), p. 121107, <https://doi.org/10.1063/1.5128231>.
- [4] M. BILOŠ, J. SOMMER, S. S. RANGAPURAM, T. JANUSCHOWSKI, AND S. GÜNNEMANN, *Neural flows: Efficient alternative to neural ODEs*, *Advances in neural information processing systems*, 34 (2021), pp. 21325–21337.
- [5] S. L. BRUNTON, J. L. PROCTOR, AND J. N. KUTZ, *Discovering governing equations from data by sparse identification of nonlinear dynamical systems*, *Proceedings of the national academy of sciences*, 113 (2016), pp. 3932–3937.
- [6] J. W. BURBY, Q. TANG, AND R. MAULIK, *Fast neural Poincaré maps for toroidal magnetic fields*, *Plasma Physics and Controlled Fusion*, 63 (2020), p. 024001, <https://doi.org/10.1088/1361-6587/abcbaa>, <http://dx.doi.org/10.1088/1361-6587/abcbaa>.
- [7] P. CANIZARES, D. MURARI, C.-B. SCHÖNLIEB, F. SHERRY, AND Z. SHUMAYLOV, *Hamiltonian matching for symplectic neural integrators*, arXiv preprint arXiv:2410.18262, (2024).

- [8] E. CELLEDONI, M. J. EHRHARDT, C. ETMANN, R. I. MCLACHLAN, B. OWREN, C.-B. SCHONLIEB, AND F. SHERRY, *Structure-preserving deep learning*, European journal of applied mathematics, 32 (2021), pp. 888–936.
- [9] E. CELLEDONI, A. LEONE, D. MURARI, AND B. OWREN, *Learning Hamiltonians of constrained mechanical systems*, Journal of Computational and Applied Mathematics, 417 (2023), p. 114608.
- [10] E. CELLEDONI, D. MURARI, B. OWREN, C.-B. SCHÖNLIEB, AND F. SHERRY, *Dynamical systems–based neural networks*, SIAM Journal on Scientific Computing, 45 (2023), pp. A3071–A3094.
- [11] R. CHEN AND M. TAO, *Data-driven prediction of general Hamiltonian dynamics via learning exactly-symplectic maps*, in Proceedings of the 38th International Conference on Machine Learning, M. Meila and T. Zhang, eds., vol. 139 of Proceedings of Machine Learning Research, PMLR, 18–24 Jul 2021, pp. 1717–1727, <https://proceedings.mlr.press/v139/chen21r.html>.
- [12] R. CHEN AND M. TAO, *Data-driven prediction of general Hamiltonian dynamics via learning exactly-symplectic maps*, in International Conference on Machine Learning, PMLR, 2021, pp. 1717–1727.
- [13] R. T. CHEN, Y. RUBANOVA, J. BETTENCOURT, AND D. K. DUVENAUD, *Neural ordinary differential equations*, Advances in neural information processing systems, 31 (2018).
- [14] Z. CHEN, J. ZHANG, M. ARJOVSKY, AND L. BOTTOU, *Symplectic recurrent neural networks*, in International Conference on Learning Representations, 2020, <https://openreview.net/forum?id=BkgYPREtPr>.
- [15] R. CORY-WRIGHT, C. CORNELIO, S. DASH, B. EL KHADIR, AND L. HORESH, *Evolving scientific discovery by unifying data and background knowledge with AI Hilbert*, Nature Communications, 15 (2024), p. 5922.
- [16] M. CRANMER, S. GREYDANUS, S. HOYER, P. BATTAGLIA, D. SPERGEL, AND S. HO, *Lagrangian neural networks*, arXiv preprint arXiv:2003.04630, (2020).
- [17] M. D. CRANMER, A. SANCHEZ-GONZALEZ, P. W. BATTAGLIA, R. XU, K. CRANMER, D. N. SPERGEL, AND S. HO, *Discovering symbolic models from deep learning with inductive biases*, CoRR, abs/2006.11287 (2020), <https://arxiv.org/abs/2006.11287>, <https://arxiv.org/abs/2006.11287>.
- [18] S. A. DESAI, M. MATTHEAKIS, D. SONDAK, P. PROTOPAPAS, AND S. J. ROBERTS, *Port-hamiltonian neural networks for learning explicit time-dependent dynamical systems*, Phys. Rev. E, 104 (2021), p. 034312, <https://doi.org/10.1103/PhysRevE.104.034312>, <https://link.aps.org/doi/10.1103/PhysRevE.104.034312>.
- [19] E. DIERKES, C. OFFEN, S. OBER-BLÖBAUM, AND K. FLASSKAMP, *Hamiltonian neural networks with automatic symmetry detection*, Chaos: An Interdisciplinary Journal of Nonlinear Science, 33 (2023).
- [20] D. DIPIETRO, S. XIONG, AND B. ZHU, *Sparse symplectically integrated neural networks*, in Advances in Neural Information Processing Systems, H. Larochelle, M. Ranzato, R. Hadsell, M. Balcan, and H. Lin, eds., vol. 33, Curran Associates, Inc., 2020, pp. 6074–6085, https://proceedings.neurips.cc/paper_files/paper/2020/file/439fca360bc99c315c5882c4432ae7a4-Paper.pdf.
- [21] M. FINZI, K. A. WANG, AND A. G. WILSON, *Simplifying hamiltonian and lagrangian neural networks via explicit constraints*, Advances in neural information processing systems, 33 (2020), pp. 13880–13889.
- [22] C. L. GALIMBERTI, L. FURIERI, L. XU, AND G. FERRARI-TRECATE, *Hamiltonian Deep Neural Networks Guaranteeing Non-vanishing Gradients by Design*, IEEE Transactions on Automatic Control, 68 (2023), pp. 3155–3162.
- [23] C. R. GALLEY, *Classical mechanics of nonconservative systems*, Physical Review Letters, 110 (2013), <https://doi.org/10.1103/physrevlett.110.174301>, <https://doi.org/10.1103%2Fphysrevlett.110.174301>.
- [24] C. R. GALLEY, D. TSANG, AND L. C. STEIN, *The principle of stationary nonconservative action for classical mechanics and field theories*, arXiv, (2014), <https://doi.org/10.48550/ARXIV.1412.3082>, <https://arxiv.org/abs/1412.3082>.
- [25] A. GRAVES AND A. GRAVES, *Supervised sequence labelling*, Springer, 2012.
- [26] S. GREYDANUS, M. DZAMBA, AND J. YOSINSKI, *Hamiltonian neural networks*, in Advances in Neural Information Processing Systems, H. Wallach, H. Larochelle, A. Beygelzimer, F. d’Alché-Buc, E. Fox, and R. Garnett, eds., vol. 32, Curran Associates, Inc., 2019, https://proceedings.neurips.cc/paper_files/paper/2019/file/26cd8ecadce0d4efd6cc8a8725cbd1f8-Paper.pdf.
- [27] T. G. GROSSMANN, U. J. KOMOROWSKA, J. LATZ, AND C.-B. SCHÖNLIEB, *Can physics-informed neural networks beat the finite element method?*, IMA Journal of Applied Mathematics, (2024), p. hxae011.

- [28] E. HAIRER, C. LUBICH, AND G. WANNER, *Geometric Numerical Integration: Structure-Preserving Algorithms for Ordinary Differential Equations*, no. 31 in Springer Series in Computational Mathematics, Springer, Berlin ; New York, 2nd ed ed., 2006.
- [29] K. HAITSIUKEVICH AND A. ILIN, *Learning trajectories of Hamiltonian systems with neural networks*, in International Conference on Artificial Neural Networks, Springer, 2022, pp. 562–573.
- [30] K. HAITSIUKEVICH AND A. ILIN, *Improved training of physics-informed neural networks with model ensembles*, in 2023 International Joint Conference on Neural Networks (IJCNN), 2023, pp. 1–8, <https://doi.org/10.1109/IJCNN54540.2023.10191822>.
- [31] J. HAN, A. JENTZEN, AND W. E, *Solving high-dimensional partial differential equations using deep learning*, Proceedings of the National Academy of Sciences, 115 (2018), pp. 8505–8510.
- [32] P. JIN, Z. ZHANG, A. ZHU, Y. TANG, AND G. E. KARNIADAKIS, *Sympnets: Intrinsic structure-preserving symplectic networks for identifying Hamiltonian systems*, Neural Networks, 132 (2020), pp. 166–179.
- [33] D. A. KALTSAS, *Constrained Hamiltonian systems and physics informed neural networks: Hamilton-Dirac neural nets*, arXiv preprint arXiv:2401.15485, (2024), <https://arxiv.org/abs/2401.15485>.
- [34] S. KARUMURI, R. TRIPATHY, I. BILIONIS, AND J. PANCHAL, *Simulator-free solution of high-dimensional stochastic elliptic partial differential equations using deep neural networks*, Journal of Computational Physics, 404 (2020), p. 109120.
- [35] A. KRISHNAPRIYAN, A. GHOLAMI, S. ZHE, R. KIRBY, AND M. W. MAHONEY, *Characterizing possible failure modes in physics-informed neural networks*, Advances in neural information processing systems, 34 (2021), pp. 26548–26560.
- [36] I. E. LAGARIS, A. LIKAS, AND D. I. FOTIADIS, *Artificial neural networks for solving ordinary and partial differential equations*, IEEE transactions on neural networks, 9 (1998), pp. 987–1000.
- [37] P.-Y. LAGRAVE AND E. TRON, *Equivariant neural networks and differential invariants theory for solving partial differential equations*, in Physical Sciences Forum, vol. 5, MDPI, 2022, p. 13.
- [38] X. LI, *Simultaneous approximations of multivariate functions and their derivatives by neural networks with one hidden layer*, Neurocomputing, 12 (1996), pp. 327–343.
- [39] T. MATSUBARA, A. ISHIKAWA, AND T. YAGUCHI, *Deep energy-based modeling of discrete-time physics*, Advances in Neural Information Processing Systems, 33 (2020), pp. 13100–13111.
- [40] M. MATTHEAKIS, D. SONDAK, A. S. DOGRA, AND P. PROTOPAPAS, *Hamiltonian neural networks for solving equations of motion*, Physical Review E, 105 (2022), p. 065305.
- [41] M. MCCABE, P. HARRINGTON, S. SUBRAMANIAN, AND J. BROWN, *Towards stability of autoregressive neural operators*, Transactions on Machine Learning Research, (2023), <https://openreview.net/forum?id=RFfUUtkYOG>.
- [42] N. MCGREIVY AND A. HAKIM, *Weak baselines and reporting biases lead to overoptimism in machine learning for fluid-related partial differential equations*, Nature Machine Intelligence, (2024), pp. 1–14.
- [43] K. MICHAŁOWSKA, S. GOSWAMI, G. E. KARNIADAKIS, AND S. RIEMER-SØRENSEN, *Neural operator learning for long-time integration in dynamical systems with recurrent neural networks*, in 2024 International Joint Conference on Neural Networks (IJCNN), IEEE, 2024, pp. 1–8.
- [44] A. PINKUS, *Approximation theory of the MLP model in neural networks*, Acta Numerica, 8 (1999), pp. 143–195.
- [45] L. POLTEROVICH, *The Geometry of the Group of Symplectic Diffeomorphisms*, Lectures in Mathematics ETH Zürich, Springer Basel AG, Basel, 2001.
- [46] M. RAISSI, P. PERDIKARIS, AND G. E. KARNIADAKIS, *Physics-informed neural networks: A deep learning framework for solving forward and inverse problems involving nonlinear partial differential equations*, Journal of Computational physics, 378 (2019), pp. 686–707.
- [47] J. SCHMIDHUBER, S. HOCHREITER, ET AL., *Long short-term memory*, Neural Comput, 9 (1997), pp. 1735–1780.
- [48] Z. SHUMAYLOV, P. ZAIKA, J. ROWBOTTOM, F. SHERRY, M. WEBER, AND C.-B. SCHÖNLIEB, *Lie algebra canonicalization: Equivariant neural operators under arbitrary lie groups*, 2024, <https://arxiv.org/abs/2410.02698>, <https://arxiv.org/abs/2410.02698>.
- [49] J. SIRIGNANO AND K. SPILIOPOULOS, *DGM: A deep learning algorithm for solving partial differential equations*, Journal of computational physics, 375 (2018), pp. 1339–1364.
- [50] A. SOSANYA AND S. GREYDANUS, *Dissipative Hamiltonian neural networks: Learning dissipative and conservative dynamics separately*, arXiv preprint arXiv:2201.10085, (2022).

- [51] S. H. STROGATZ, *Nonlinear Dynamics and Chaos: With Applications to Physics, Biology, Chemistry, and Engineering*, CRC press, 2018.
- [52] L. SUN, H. GAO, S. PAN, AND J.-X. WANG, *Surrogate modeling for fluid flows based on physics-constrained deep learning without simulation data*, *Computer Methods in Applied Mechanics and Engineering*, 361 (2020), p. 112732.
- [53] B. K. TAPLEY, *Symplectic neural networks based on dynamical systems*, arXiv preprint arXiv:2408.09821, (2024).
- [54] Y. TONG, S. XIONG, X. HE, G. PAN, AND B. ZHU, *Symplectic neural networks in Taylor series form for Hamiltonian systems*, *Journal of Computational Physics*, 437 (2021), p. 110325.
- [55] D. TSANG, C. R. GALLEY, L. C. STEIN, AND A. TURNER, “*Slimplectic*” *Integrators: Variational Integrators for General Nonconservative Systems*, *The Astrophysical Journal*, 809 (2015), p. L9, <https://doi.org/10.1088/2041-8205/809/1/19>.
- [56] D. TURAEV, *Polynomial approximations of symplectic dynamics and richness of chaos in non-hyperbolic area-preserving maps*, *Nonlinearity*, 16 (2002), p. 123.
- [57] R. WANG AND R. YU, *Physics-guided deep learning for dynamical systems: A survey*, arXiv preprint arXiv:2107.01272, (2021).
- [58] S. WANG AND P. PERDIKARIS, *Long-time integration of parametric evolution equations with physics-informed DeepONets*, *Journal of Computational Physics*, 475 (2023), p. 111855.
- [59] S. XIONG, Y. TONG, X. HE, S. YANG, C. YANG, AND B. ZHU, *Nonseparable symplectic neural networks*, in *International Conference on Learning Representations*, 2021, <https://openreview.net/forum?id=B5VvQrI49Pa>.
- [60] L. ZHANG, Y. CHENG, L. LIU, C.-B. SCHÖNLIEB, AND A. I. AVILES-RIVERO, *Biophysics informed pathological regularisation for brain tumour segmentation*, arXiv preprint arXiv:2403.09136, (2024).
- [61] Z. ZHANG, C. WANG, S. LIU, J. DARBON, AND G. KARNIADAKIS, *A time-dependent symplectic network for non-convex path planning problems with linear and nonlinear dynamics*, 2024, <https://arxiv.org/abs/2408.03785>, <https://arxiv.org/abs/2408.03785>.
- [62] Y. D. ZHONG, B. DEY, AND A. CHAKRABORTY, *Dissipative symODEN: Encoding hamiltonian dynamics with dissipation and control into deep learning*, in *ICLR 2020 Workshop on Integration of Deep Neural Models and Differential Equations*, 2019, <https://openreview.net/forum?id=knjWfN6CN>.
- [63] Y. D. ZHONG, B. DEY, AND A. CHAKRABORTY, *Symplectic ODE-Net: Learning Hamiltonian dynamics with control*, in *International Conference on Learning Representations*, 2020, <https://openreview.net/forum?id=ryxmb1rKDS>.
- [64] Y. ZHU, N. ZABARAS, P.-S. KOUTSOURELAKIS, AND P. PERDIKARIS, *Physics-constrained deep learning for high-dimensional surrogate modeling and uncertainty quantification without labeled data*, *Journal of Computational Physics*, 394 (2019), pp. 56–81.

A The classical mechanics of non-conservative systems: Damped Harmonic Oscillator

In this section, we summarize the non-conservative Hamiltonian formulation used to extend SympFlow to dissipative systems [23, 24, 55]. This approach enables the modeling of dissipative dynamics as a canonical Hamiltonian system but does not inherently preserve symplecticity. We outline the key aspects of this formulation and detail the modifications required to ensure symplecticity, allowing its integration into SympFlow.

The starting point of the non-conservative Hamiltonian formulation [23] is to move from the system’s phase space to an augmented one, which is obtained by doubling the degrees of freedom, and back to the original space. The main idea is to capture the dissipative evolution in this augmented phase-space, ensuring that the global dynamics of the system is conservative. Hence, the configuration variable q , and the momentum p are doubled giving rise to two different curves each: $q \rightarrow (q_a, q_b)$ and $p \rightarrow (p_a, p_b)$. In this framework, a new non-conservative Lagrangian is derived from the augmented action with doubled variables:

$$\mathcal{S} = \int \Lambda(q_{a,b}, \dot{q}_{a,b}, t) dt \quad (27)$$

where the (non-conservative) Lagrangian is defined by:

$$\Lambda(q_{a,b}, \dot{q}_{a,b}, t) = L(q_a, \dot{q}_a, t) - L(q_b, \dot{q}_b, t) + K(q_{a,b}, \dot{q}_{a,b}, t),$$

where L describes the conservative contribution to the full non-conservative Lagrangian Λ , and K is an antisymmetric function under exchange $a \rightarrow b$, that couples the variables together and accounts for all the non-conservative contribution to the system dynamics. Notice that, in conservative Hamiltonian systems, the function K would vanish. Although, K also vanishes in the physical limit (PL) [23], that is, in the linear subspace $\{(q_a, q_b, p_a, p_b) \in \mathbb{R}^{4d} : q_a = q_b, \text{ and } p_a = p_b\}$, its derivatives do not necessarily vanish in the physical limit. This is important, since the derivatives of K model the dissipative behavior of the system, as we will see below.

The stationarity of the action in Equation (27) under the variations $q_I(t, \epsilon) = q_I(t, 0) + \epsilon \eta_I(t)$, that is $[dS[q_I]/d\epsilon]_{\epsilon=0} = 0$ for all $\eta_I(t_i) = \eta_I(t_f) = 0$, $I = \{a, b\}$, corresponds to the conditions

$$\begin{aligned} 0 &= \int_{t_i}^{t_f} \left\{ \left[\frac{\partial \Lambda}{\partial q_a} \frac{\partial q_a}{\partial \epsilon} + \frac{\partial \Lambda}{\partial \dot{q}_a} \frac{\partial \dot{q}_a}{\partial \epsilon} + \frac{\partial \Lambda}{\partial q_b} \frac{\partial q_b}{\partial \epsilon} + \frac{\partial \Lambda}{\partial \dot{q}_b} \frac{\partial \dot{q}_b}{\partial \epsilon} \right]_{\epsilon=0} \right\} dt \\ &= \int_{t_i}^{t_f} \left\{ \eta_a \cdot \left[\frac{\partial \Lambda}{\partial q_a} - \frac{d\pi_a}{dt} \right]_{\epsilon=0} + \eta_b \cdot \left[\frac{\partial \Lambda}{\partial q_b} + \frac{d\pi_b}{dt} \right]_{\epsilon=0} \right\} dt \\ &\quad + \left[\eta_a(t) \cdot \pi_b(t) - \eta_b(t) \cdot \pi_a(t) \right]_{t=t_i}^{t_f} \end{aligned} \quad (28)$$

where the quantities π_I are the (non-conservative) conjugate momenta, defined by:

$$\pi_a(q_I, \dot{q}_I, t) = \frac{\partial \Lambda(q_I, \dot{q}_I, t)}{\partial \dot{q}_a(t)} = \frac{\partial L(q_a, \dot{q}_a, t)}{\partial \dot{q}_a} + \frac{\partial K(q_I, \dot{q}_I, t)}{\partial \dot{q}_a} \quad (29)$$

$$\pi_b(q_I, \dot{q}_I, t) = \frac{\partial \Lambda(q_I, \dot{q}_I, t)}{\partial \dot{q}_b} = -\frac{\partial L(q_b, \dot{q}_b, t)}{\partial \dot{q}_b} + \frac{\partial K(q_I, \dot{q}_I, t)}{\partial \dot{q}_b} \quad (30)$$

In [23], the authors choose a different sign convention for the momenta hence working with Hamiltonian equations associated to a non-canonical symplectic structure over \mathbb{R}^{4d} . Our choice for the sign of p is due to the fact that `SympFlow` preserves the canonical symplectic form of \mathbb{R}^{4d} . With this sign convention, the physical limit expressed with respect to the momenta corresponds to the subspace given by:

$$\{(q_a, q_b, \pi_a, \pi_b) \in \mathbb{R}^{4d} : q_a = q_b, \text{ and } \pi_a = -\pi_b\}. \quad (31)$$

We remark that $\pi_a = -\pi_b$ can be inferred e.g. in the case of a damped harmonic oscillator below by noticing that $\pi_a + \pi_b = p_a - p_b - \lambda(q_a - q_b) = 0$, where p_a and p_b are the conservative momenta derived from the conservative Lagrangian as $p_I = \partial_{\dot{q}_I} L(q_I, \dot{q}_I)$, $I \in \{a, b\}$.

In the damped harmonic oscillator example, we consider a dissipative potential of the form $K = -\frac{\lambda}{2}(\dot{q}_a + \dot{q}_b)(q_a - q_b)$ [55] (see [24] for other choices). The corresponding (non-conservative) Lagrangian is, then, given by:

$$\Lambda(q_I, \dot{q}_I) = \left(\frac{m}{2} \dot{q}_a^2 - \frac{k}{2} q_a^2 \right) - \left(\frac{m}{2} \dot{q}_b^2 - \frac{k}{2} q_b^2 \right) - \frac{\lambda}{2} (\dot{q}_a + \dot{q}_b) (q_a - q_b), \quad (32)$$

where k is the oscillator's recovery constant, and λ is the dissipation factor. The corresponding (non-conservative) conjugate momenta for each double variable are then given by:

$$\pi_a = \frac{\partial \Lambda(q_I, \dot{q}_I)}{\partial \dot{q}_a} = m\dot{q}_a - \frac{\lambda}{2}(q_a - q_b) = p_a - \frac{\lambda}{2}(q_a - q_b) \quad (33)$$

$$\pi_b = \frac{\partial \Lambda(q_I, \dot{q}_I)}{\partial \dot{q}_b} = -m\dot{q}_b - \frac{\lambda}{2}(q_a - q_b) = -p_b - \frac{\lambda}{2}(q_a - q_b). \quad (34)$$

That is, the non-conservative momenta are given by the conservative ones p_a, p_b , plus an extra term due to the dissipative contribution. We also remark that, in the physical limit, $\pi_a = p_a$ and $\pi_b = -p_b$.

The non-conservative (augmented) Hamiltonian is obtained by applying the Legendre transform to the non-conservative Lagrangian Λ :

$$\begin{aligned} A(t, q_a, q_b, \pi_a, \pi_b) &= \frac{1}{2m}(\pi_a^2 - \pi_b^2) + \frac{\lambda}{2m}(q_a - q_b)(\pi_a - \pi_b) \\ &\quad + \frac{k}{2}(q_a - q_b)(q_a + q_b). \end{aligned}$$

Hence, the final Hamiltonian equations for the damped harmonic oscillator in the augmented space are given by:

$$\begin{bmatrix} \dot{q}_a(t) \\ \dot{q}_b(t) \\ \dot{p}_1(t) \\ \dot{p}_2(t) \end{bmatrix} = \begin{bmatrix} \frac{\pi_a(t)}{m} + \frac{\lambda}{2m}(q_a(t) - q_b(t)) \\ -\frac{\pi_b(t)}{m} - \frac{\lambda}{2m}(q_a(t) - q_b(t)) \\ -\frac{\lambda}{2m}(\pi_a(t) - \pi_b(t)) - kq_a(t) \\ \frac{\lambda}{2m}(\pi_a(t) - \pi_b(t)) + kq_b(t) \end{bmatrix}. \quad (35)$$

Notice that the physical limit in Equation (31) is an invariant submanifold of \mathbb{R}^{4d} with respect to the dynamics, since $\dot{\pi}_a + \dot{\pi}_b = 0$ whenever $q_a = q_b$, and also $\dot{q}_a - \dot{q}_b = 0$. To ensure that our neural networks preserve this subspace as well, we apply a projection step at the end of the network, which projects over the subspace in Equation (31) and is defined as

$$[q_a \quad q_b \quad \pi_a \quad \pi_b] \mapsto \left[\frac{q_a + q_b}{2} \quad \frac{q_a + q_b}{2} \quad \frac{\pi_a - \pi_b}{2} \quad -\frac{\pi_a - \pi_b}{2} \right].$$

We remark that this projection turns the `SympFlow` into a non-symplectic map in this context, but it is not important since the actual physical system we are integrating is not a conservative Hamiltonian system. The symplectic structure encoded in the network still seems to improve the approximation accuracy, as we show in the numerical experiments Section 4.

Similarly, the equations of motion for the double variables (q_a, q_b, p_a, p_b) are given by:

$$\dot{p}_a = \dot{\pi}_a + \frac{\lambda}{2}(\dot{q}_a - \dot{q}_b) = -\frac{\lambda}{m}p_2 - kq_a \quad (36)$$

$$\dot{p}_b = -\dot{\pi}_b + \frac{\lambda}{2}(\dot{q}_a - \dot{q}_b) = -\frac{\lambda}{m}p_b - kq_b. \quad (37)$$

$$\dot{q}_a = \frac{\lambda}{2m}(q_a - q_b) + \frac{p_a}{m} - \frac{\lambda}{2m}(q_a - q_b) = \frac{p_a}{m} \quad (38)$$

$$\dot{q}_b = -\frac{\lambda}{2m}(q_a - q_b) + \frac{p_b}{m} + \frac{\lambda}{2m}(q_a - q_b) = \frac{p_b}{m}. \quad (39)$$

Notice that in the figures in this paper the letters p_a and p_b denote the momenta. We emphasize that these momenta are the non-conservative ones, since they are the result of solving the augmented system. However, because of the projection, they coincide with the conservative ones, i.e., $\pi_a = p_a$ and $-\pi_b = p_b$, hence why we use this convention as discussed above.

B Derivation of the long-time Hamiltonian system

Let us consider the function

$$\psi(t, x_0) := \bar{\psi}_{t-\Delta t \lfloor t/\Delta t \rfloor} \circ (\bar{\psi}_{\Delta t})^{\lfloor t/\Delta t \rfloor}(x_0),$$

and evaluate its derivative in time. We evaluate the following limit

$$\dot{\psi}(t, x_0) = \lim_{h \rightarrow 0} \frac{\psi(t+h, x_0) - \psi(t, x_0)}{h}$$

where we notice that if $t \neq k\Delta t$, $k \in \mathbb{N}$, one has that $\lfloor (t+h)/\Delta t \rfloor = \lfloor t/\Delta t \rfloor$ as long as h is small enough. Thus, setting $c = \lfloor t/\Delta t \rfloor$, we get

$$\begin{aligned} \dot{\psi}(t, x_0) &= \lim_{h \rightarrow 0} \frac{\bar{\psi}_{t+h-c\Delta t}((\bar{\psi}_{\Delta t})^c(x_0)) - \bar{\psi}_{t-c\Delta t}((\bar{\psi}_{\Delta t})^c(x_0))}{h} \\ &= \mathbf{J}\nabla\mathcal{H}(\bar{\psi})(t - c\Delta t, \psi(t, x_0)) \end{aligned}$$

as written in Equation (13).

C Proof of the a-posteriori result

Proof of Theorem 2. To start, we notice that

$$\begin{aligned} \mathcal{H}(\psi)(t, x) &= \mathcal{H}(\bar{\psi})(t - \Delta t \lfloor t/\Delta t \rfloor, x) \\ &= H(x) + \delta(t - \Delta t \lfloor t/\Delta t \rfloor, x) \end{aligned}$$

for some function $\delta : [0, \Delta t] \times \mathbb{R}^{2d} \rightarrow \mathbb{R}$ with $|\delta(t, x)| \leq \varepsilon_1$ for every $t \in [0, \Delta t]$, $x \in \Omega$. In this proof, when using the symbol ∇ we always refer to the gradient with respect to the second input. By the second assumption, on the smallness of the residual, we know that

$$\|\mathbf{J}\nabla\mathcal{H}(\psi)(t, \psi_t(x)) - \mathbf{J}\nabla H(\psi_t(x))\|_2 \leq \varepsilon_2,$$

and since \mathbf{J} preserves the ℓ^2 norm, we get that $\|\nabla\delta(t, x)\|_2 \leq \varepsilon_2$ too. This allows us to conclude that

$$\frac{d}{dt} H(\psi_t(x)) = \nabla H(\psi_t(x)) \cdot \mathbf{J}\nabla\delta(t - \Delta t \lfloor t/\Delta t \rfloor, \psi_t(x)) \leq C\varepsilon_2,$$

where C is an upper bound of the Lipschitz constant of H over Ω . Thus,

$$|H(\psi_t(x)) - H(x)| \leq c_2\varepsilon_2 t.$$

Moving to the variation of $\mathcal{H}(\psi)$, we notice that

$$\begin{aligned}\mathcal{H}(\psi)(t, \psi_t(x)) - \mathcal{H}(\psi)(0, x) &= \mathcal{H}(\psi)(t, \psi_t(x)) - H(\psi_t(x)) \\ &\quad + H(\psi_t(x)) - H(x) \\ &\quad + H(x) - \mathcal{H}(\psi)(0, x),\end{aligned}$$

which allows us to conclude

$$|\mathcal{H}(\psi)(t, \psi_t(x)) - \mathcal{H}(\psi)(0, x)| \leq 2\varepsilon_1 + c_2\varepsilon_2t \leq \max\{2, c_2\}(\varepsilon_1 + \varepsilon_2t) =: c_1(\varepsilon_1 + \varepsilon_2t).$$

□

D Proof of Theorem 1

This appendix provides a proof of Theorem 1, i.e., that any Hamiltonian flow can be approximated to arbitrary accuracy, uniformly on a compact time interval $[0, \Delta t]$, by a suitable `SympFlow`. Our proof builds on the derivations in [56].

Step 1: Approximation with polynomials

Lemma 1 (Approximation with polynomial Hamiltonian). *Let $H : \mathbb{R} \times \Omega \rightarrow \mathbb{R}$ be a C^1 function, for $\Omega \subset \mathbb{R}^{2d}$ compact representing the phase space, while the first parameter denotes time. For any $\varepsilon > 0$, there is a function $\tilde{H} : \mathbb{R} \times \Omega \rightarrow \mathbb{R}$ polynomial in the phase-space variable $x \in \Omega$ and with coefficients continuously depending on time, whose exact flow $\phi_{\tilde{H}, t}$ approximates $\phi_{H, t}$ to accuracy ε on $\Omega \times [0, \Delta t]$.*

Proof. The function H is a continuous function of the $2d + 1$ variables $(x, t) \in \Omega \times [0, \Delta t]$. Hence, it can be approximated to arbitrary accuracy on the compact set $\Omega \times [0, \Delta t]$ by a polynomial in (x, t) . The approximating polynomial can be chosen to also approximate the gradient of H with the same accuracy. For a proof of this result see [38, Proposition 4.2].

Let us consider now a polynomial function \tilde{H} giving

$$\sup_{\substack{t \in [0, \Delta t] \\ x \in \Omega}} \left\| \nabla H(t, x) - \nabla \tilde{H}(t, x) \right\|_{\infty} < \tilde{\varepsilon}.$$

Then, we have that

$$\begin{aligned}\left\| \phi_{H, t}(x) - \phi_{\tilde{H}, t}(x) \right\|_{\infty} &= \left\| \mathbf{J} \int_0^t \left(\nabla H(s, \phi_{H, s}(x)) - \nabla \tilde{H}(s, \phi_{\tilde{H}, s}(x)) \right) ds \right\|_{\infty} = \\ &= \left\| \mathbf{J} \int_0^t \left(\nabla H(s, \phi_{H, s}(x)) - \nabla H(s, \phi_{\tilde{H}, s}(x)) + \nabla H(s, \phi_{\tilde{H}, s}(x)) - \nabla \tilde{H}(s, \phi_{\tilde{H}, s}(x)) \right) ds \right\|_{\infty} \\ &\leq \left(\sup_{\substack{s \in [0, \Delta t] \\ x \in \Omega}} \left\| \nabla^2 H(s, x) \right\|_{\infty} \right) \int_0^t \left\| \phi_{H, s}(x) - \phi_{\tilde{H}, s}(x) \right\|_{\infty} ds + \tilde{\varepsilon} \Delta t.\end{aligned}$$

Grownall's inequality allows us to conclude that

$$\begin{aligned}\left\| \phi_{H, t}(x) - \phi_{\tilde{H}, t}(x) \right\|_{\infty} &\leq \tilde{\varepsilon} \Delta t \exp \left(t \sup_{\substack{s \in [0, \Delta t] \\ x \in \Omega}} \left\| \nabla^2 H(s, x) \right\|_{\infty} \right) \\ &\leq \tilde{\varepsilon} \Delta t \exp \left(\Delta t \sup_{\substack{s \in [0, \Delta t] \\ x \in \Omega}} \left\| \nabla^2 H(s, x) \right\|_{\infty} \right) =: \tilde{\varepsilon} \Delta t \exp(\Delta t L).\end{aligned}$$

The lemma is proven by taking $\tilde{\varepsilon} = \varepsilon / (\Delta t \exp(\Delta t L))$, where L is a bound for the Lipschitz constant of $\nabla H(s, \cdot)$ uniform in $s \in [0, \Delta t]$. □

Step 2: Splitting of the exact flow in N substeps

Thanks to Lemma 1, we can now assume to work with $\tilde{H} : \mathbb{R} \times \Omega \rightarrow \mathbb{R}$ which is a polynomial in the phase-space variable x and with coefficients continuously depending on time. We can then split the flow $\phi_{\tilde{H},t}$ into N substeps of size t/N as follows:

$$\phi_{\tilde{H},t} = \tilde{\phi}_{(N-1)t/N} \circ \dots \circ \tilde{\phi}_{nt/N} \circ \dots \circ \tilde{\phi}_0, \quad n = 0, \dots, N-1. \quad (40)$$

In Equation (40), we denote with $\tilde{\phi}_{nt/N}(x_0)$ the exact solution at time $(n+1)t/N$ of the initial value problem

$$\begin{cases} \frac{dx(s)}{ds} = \mathbf{J} \nabla_x \tilde{H}(s, x) \\ x(nt/N) = x_0. \end{cases}$$

Step 3: Approximation via a separable Hamiltonian system

The goal is now getting closer to the form of differential equations defining the layers of the SympFlow. To do so, we work with [56, Lemma 1], which we now state adapting the notation to ours.

Lemma 2 (Lemma 1 in [56]). *Let $\tilde{H} : \mathbb{R} \times \Omega \rightarrow \mathbb{R}$ be polynomial in the phase-space variable $x \in \Omega$ and depending continuously on the first variable. There exists a function $V : \mathbb{R} \times \mathbb{R}^d \rightarrow \mathbb{R}$ polynomial in the second variable and with coefficients depending continuously on the first variable and a set of d integers $\omega_1, \dots, \omega_d$, such that the Hamiltonian*

$$\hat{H}(s, x) = \frac{1}{2} \left(\|p\|_2^2 + 2\pi q^\top \text{diag}(\omega_1^2, \dots, \omega_d^2) q \right) + \frac{t}{N} V(s, q), \quad x = (q, p) \in \mathbb{R}^{2d}, \quad (41)$$

whose exact time-1 flow $\phi_{\hat{H},1}$ is $\mathcal{O}(t^2/N^2)$ close to $\tilde{\phi}_{nt/N}$.

We do not specify it in the notation since it is already quite heavy, but this approximation depends on the time instant nt/N , so \hat{H} would be \hat{H}_n . We remark that the differential equation defined by \hat{H} in Equation (41) is a second-order differential equation of the form

$$\frac{d^2}{ds^2} q(s) = -2\pi \text{diag}(\omega_1^2, \dots, \omega_d^2) q(s) - \frac{t}{N} \nabla_q V(s, q(s)). \quad (42)$$

For this reason, the proof in [56] is based on a perturbative argument studying Equation (42) as a perturbation of the linear oscillator obtained by removing the non-linear potential V .

An equivalent way to write Equation (42) is with the first-order differential equation

$$\begin{bmatrix} \dot{q}(s) \\ \dot{p}(s) \end{bmatrix} = \begin{bmatrix} p(s) \\ -2\pi \text{diag}(\omega_1^2, \dots, \omega_d^2) q(s) - \frac{t}{N} \nabla_q V(s, q(s)) \end{bmatrix}. \quad (43)$$

Corollary 1. *Let $\tilde{H} : \mathbb{R} \times \Omega \rightarrow \mathbb{R}$ be polynomial in the phase-space variable $x \in \Omega$ and depending continuously on the first variable. For every $\varepsilon > 0$, there exists a pair of functions $\bar{V}_q, \bar{V}_p \in \mathcal{F}$, with*

$$\mathcal{F} = \left\{ \mathbb{R} \times \mathbb{R}^d \ni (s, q) \mapsto w^\top \sigma(Aq + bs + c) \in \mathbb{R} : A \in \mathbb{R}^{h \times d}, b, c, w \in \mathbb{R}^h, h \in \mathbb{N} \right\},$$

$\sigma : \mathbb{R} \rightarrow \mathbb{R}$ continuously differentiable and not a polynomial, such that defined the Hamiltonian

$$\bar{H}(s, x) = \bar{V}_p(s, p) + \bar{V}_q(s, q), \quad x = (q, p) \in \mathbb{R}^{2d}, \quad (44)$$

the exact time-1 flow $\phi_{\bar{H},1}$ is ε close to $\tilde{\phi}_{nt/N}$.

Lemma 2 is fundamental to prove Corollary 1 since we need to get a separable Hamiltonian, so that we can relate these maps with a SympFlow. Jumping over Lemma 2 would have required a significantly new analysis to directly obtain Corollary 1.

Proof. By [44, Theorem 4.1], for any $\tilde{\varepsilon} > 0$ there are two functions $\bar{V}_q = \bar{V}_q(s, q)$ and $\bar{V}_p = \bar{V}_p(s, p)$ that belong to \mathcal{F} and such that

$$\sup_{\substack{s \in [0,1] \\ x \in \Omega}} \left\| \nabla \hat{H}(s, x) - \nabla \bar{H}(s, x) \right\|_\infty < \tilde{\varepsilon},$$

where \bar{H} is defined as in Equation (44), and \hat{H} as in Equation (41). This is a consequence of the fact that polynomials are continuous functions, and \mathcal{F} is dense in the space of continuously differentiable scalar valued functions with respect to the C^1 -topology. The proof can then be concluded by Gronwall's inequality as in the proof of Lemma 1 \square

We remark that in particular one can take $\varepsilon = t^2/N^2$ and get the same approximation accuracy as in Lemma 2.

Step 4: Approximation of $\phi_{\bar{H},1}$ with a SympFlow

To conclude, we need to show that the flow map $\phi_{\bar{H},1}$ with \bar{H} defined as in Equation (44) can be approximated by a suitable SympFlow. To do so, we apply the decomposition in Equation (40) to $\phi_{\bar{H},1}$. We split the time interval $[0, 1]$ into K substeps, leading to substeps that we denote as $\bar{\phi}_{k/K}$ associated to the integration interval $[k/K, (k+1)/K]$, with $k = 0, \dots, K-1$. We can then approximate $\bar{\phi}_{k/K}$ up to $\mathcal{O}(1/K^2)$ with a 1-layer SympFlow obtained by applying a Lie-Trotter splitting strategy to Equation (43). More explicitly, we can write

$$\bar{\phi}_{k/K} = \phi_{\bar{H}_1,1/K} \circ \phi_{\bar{H}_2,1/K} + \mathcal{O}\left(\frac{1}{K^2}\right), \quad (45)$$

with $\bar{H}_1(s, x) = \bar{V}_p(s, p)$ and $\bar{H}_2(s, x) = \bar{V}_q(s, q)$, see Corollary 1. Having K of these sub-steps, we can thus conclude that there exists a SympFlow of at most K layers able to approximate within $\mathcal{O}(1/K)$ the time-1 flow $\phi_{\bar{H},1}$. This error accumulation is due to the fact that we compose K maps $\mathcal{O}(1/K^2)$ close to the reference one. Thus, we have a global error growing like $1/K$. The \mathcal{O} notation hides the multiplicative constants, which depend on the Lipschitz regularity of the flow maps.

Step 5: Combining all the approximations to conclude the proof

We can now conclude the proof by combining the various approximations done in the previous steps and using the fact that the composition of SympFlows is again a SympFlow. We first recall the decomposition

$$\phi_{\tilde{H},t} = \tilde{\phi}_{(N-1)t/N} \circ \dots \circ \tilde{\phi}_{nt/N} \circ \dots \circ \tilde{\phi}_0, \quad n = 0, \dots, N-1.$$

In steps 3 and 4 we showed that for each $n = 0, \dots, N-1$ there is a SympFlow of at most K layers approximating within $\mathcal{O}(1/K)$ the exact flow $\phi_{\tilde{H},1}$, which is known to be $\mathcal{O}(\Delta t^2/N^2)$ close to $\tilde{\phi}_{nt/N}$, see Corollary 1. If we set $K = N^2$, we can thus conclude that the map $\phi_{\tilde{H},t}$, and hence also $\phi_{H,t}$, can be approximated within $\mathcal{O}(\Delta t^2/N)$ by a SympFlow of at most N^3 layers. N can then be selected based on the desired accuracy ε . This reasoning works assuming that Δt is of moderate size, like $\Delta t = 1$ we use in our experiments. Otherwise, one would have to slightly modify the reasoning.

E Description of the network architectures

In what follows, we provide details on the network architectures considered in Section 4. All the networks we compare have the same number of layers, where each layer is defined as a transformation acting on both parts, q and p , which partition the phase-space variable $x \in \mathbb{R}^{2d}$. The number of layers chosen in the numerical experiments in Section 4 is based on SympFlow's performance. Thus, in the unsupervised experiments, the number of layers is set to three, whereas in the supervised experiments is set to five. Additionally, in all experiments the activation function is $\sigma = \tanh$.

Although we have set the MLP to have the same number of layers than SympFlow, the highly constrained architecture of SympFlow results in a greater number of network parameters compared to the MLP. Nevertheless, we consider this comparison fair because, in all numerical experiments, the MLP accurately approximates the target map just as well as SympFlow over $\Omega \times [0, \Delta t]$. This demonstrates that the poor long-term behavior of the MLP is not due to a lack of expressive power but rather to its lack of a symplectic structure.

E.1 SympFlow

Given a SympFlow, the i -th layer of $\tilde{\psi}_t$ is given by the composition map $\phi_p^i \circ \phi_q^i$. Each of these two composed maps depends on network weights only via a potential function, which is denoted as V_q^i and V_p^i . We model both potential functions with a one-hidden layer feedforward neural network. We explicit it for V_q^i , and the same applies to V_p^i , possibly with different weights:

$$V_q(t, q) = \ell_3 \circ \sigma \circ \ell_2 \circ \sigma \circ \ell_1 \left(\begin{bmatrix} q \\ t \end{bmatrix} \right),$$

where

$$\ell_1 : \mathbb{R}^{d+1} \rightarrow \mathbb{R}^h, \quad \ell_2 : \mathbb{R}^h \rightarrow \mathbb{R}^h, \quad \ell_3 : \mathbb{R}^h \rightarrow \mathbb{R},$$

$h = 10$, are three parametrized affine maps of the form $\ell_j(x) = A_j x + b_j$ for suitably shaped weight A_j and bias b_j , $j = 1, 2, 3$. For the case of the simple harmonic oscillator, where $d = 1$, we thus have 30 parameters modeling ℓ_1 , 110 modeling ℓ_2 , and 11 modeling ℓ_3 . A SympFlow of 5 layers will hence have $5 \cdot 2 \cdot (30 + 110 + 11) = 1510$ parameters.

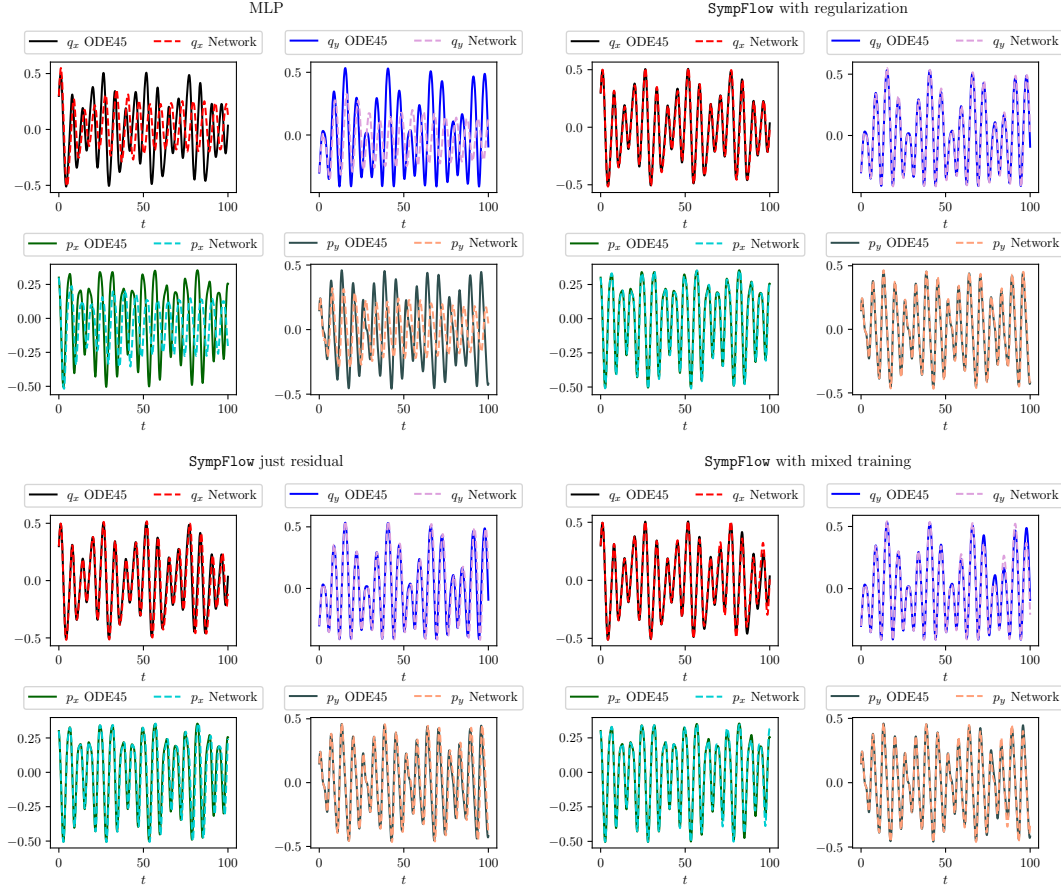


Figure 12: **Unsupervised experiment — Hénon–Heiles**: Comparison of the solutions obtained with the different methods, with integration time $[0, T = 100]$.

E.2 MLP

An MLP with $L \in \mathbb{N}$ layers is based on a parametric maps of the form

$$\varphi_i : \mathbb{R}^{c_i} \rightarrow \mathbb{R}^{c_{i+1}}, \quad \varphi_i(z) = \sigma \circ \ell_i(z), \quad i = 1, \dots, L, \quad (46)$$

for an affine map parametrized as $\ell_i(z) = A_i z + b_i$, $A_i \in \mathbb{R}^{c_{i+1} \times c_i}$ and $b_i \in \mathbb{R}^{c_{i+1}}$. For the first layer we have $c_i = 2d + 1$, since

$$z = \begin{bmatrix} x \\ t \end{bmatrix},$$

whereas for the last layer $c_{L+1} = 2d$. All the intermediate dimensions are fixed to $c_2 = \dots = c_L = 10$. For the simple harmonic oscillator, considering an MLP of 5 layers, we thus have that the first layer is parametrized by 40 parameters, the intermediate three by 110 each, and the last by 22. This leads to a network with $40 + 330 + 22 = 392$ parameters.

Since composing maps as in Equation (46) does not allow to enforce the initial condition, we modify the composition and define the MLP network as

$$\bar{\psi}(t, x) = x + \tanh(t) \cdot \varphi_L \circ \dots \circ \varphi_1 \left(\begin{bmatrix} x \\ t \end{bmatrix} \right),$$

so that $\bar{\psi}(0, x) = x$ for every $x \in \mathbb{R}^{2d}$ since $\tanh(0) = 0$.

F Additional experiments for Hénon–Heiles

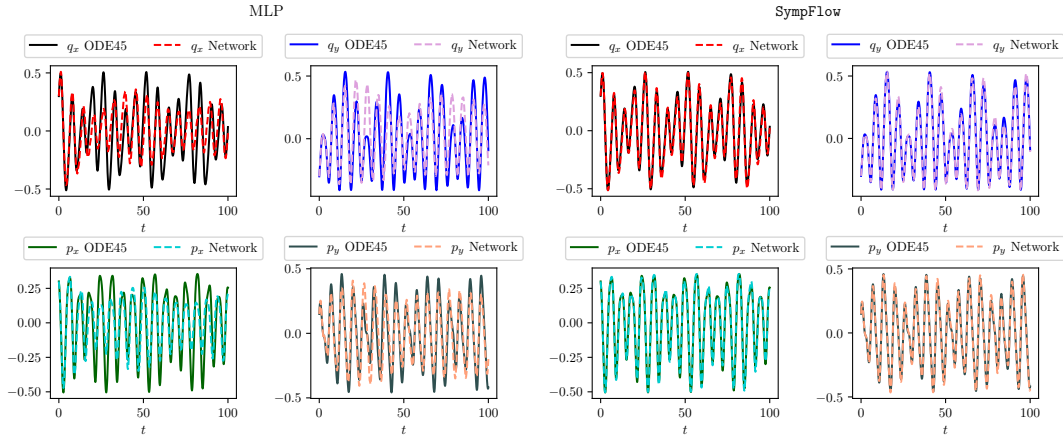


Figure 13: **Supervised experiment — Hénon-Heiles:** Comparison of the solutions obtained with the different methods, with integration time $[0, T = 100]$.

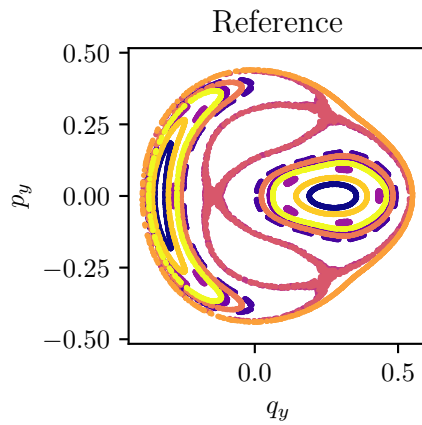


Figure 14: Poincaré section for Hénon-Heiles obtained with Runge-Kutta (5,4) time integration.